

Shear viscosity and electric conductivity of a hot and dense QGP with a chiral phase transitionOlga Soloveva¹, David Fuseau,² Jörg Aichelin,² and Elena Bratkovskaya^{1,3,4,*}¹*Institut für Theoretische Physik, Johann Wolfgang Goethe-Universität, Max-von-Laue-Straße 1, D-60438 Frankfurt am Main, Germany*²*SUBATECH, University of Nantes, IMT Atlantique, IN2P3/CNRS, 4 Rue Alfred Kastler, 44307 Nantes Cedex 3, France*³*GSI Helmholtzzentrum für Schwerionenforschung GmbH, Planckstraße 1, D-64291 Darmstadt, Germany*⁴*Helmholtz Research Academy Hessen for FAIR (HFHF), GSI Helmholtz Center for Heavy Ion Physics, Campus Frankfurt, D-60438 Frankfurt, Germany*

(Received 9 November 2020; revised 24 March 2021; accepted 12 April 2021; published 4 May 2021)

We calculate two transport coefficients—the shear viscosity over entropy ratio η/s and the ratio of the electric conductivity to the temperature, σ_0/T —of strongly interacting quark matter within the extended $N_f = 3$ Polyakov Nambu-Jona-Lasinio (PNJL) model along the crossover transition line for moderate values of baryon chemical potential $0 \leq \mu_B \leq 0.9$ GeV as well as in the vicinity of the critical endpoint (CEP) and at large baryon chemical potential $\mu_B = 1.2$ GeV, where the first-order phase transition takes place. The evaluation of the transport coefficients is performed on the basis of the effective Boltzmann equation in the relaxation time approximation. We employ two different methods for the calculation of the quark relaxation times: (i) using the averaged transition rate defined via thermal averaged quark-quark and quark-antiquark PNJL cross sections and (ii) using the “weighted” thermal averaged quark-quark and quark-antiquark PNJL cross sections. The η/s and σ_0/T transport coefficients have similar temperature and chemical potential behaviors when approaching the chiral phase transition for both methods for the quark relaxation time; however, the differences grow with increasing temperature. We demonstrate the effect of the first-order phase transition and of the CEP on the transport coefficients in the deconfined QCD medium.

DOI: [10.1103/PhysRevC.103.054901](https://doi.org/10.1103/PhysRevC.103.054901)**I. INTRODUCTION**

Understanding the nature of a possible phase transition and the properties of the quark-gluon plasma (QGP) produced in relativistic heavy-ion collisions [1–3] is presently one of the most challenging questions in the physics of strong interactions. State-of-the-art lattice QCD (lQCD) calculations allow for the evaluation of the thermal properties of the QGP at vanishing baryon chemical potential (μ_B). For finite baryon chemical potential one has to rely on phenomenological models. Moreover, for the calculation of transport coefficients one has to advance to transport theories which describe the expansion of the QGP. The experimental exploration of the finite μ_B region of the QCD phase diagram is one of the primary goals of the Beam Energy Scan programs of the Relativistic Heavy Ion Collider (RHIC) at BNL [4] as well as of the planned experimental program of FAIR (Facility for Antiproton and Ion Research) [5] at GSI and of NICA (Nuclotron-based Ion Collider fAcility) at JINR [6].

In a hot and dense environment it is notoriously difficult to calculate microscopic properties of the QGP from first principles [7]. The expansion and dilution of the quark medium, produced in nuclear collisions, is usually described by relativistic viscous hydrodynamics, which contains transport coefficients in the dissipative part. Although the hydrodynamic equations provide a macroscopic description of a

relativistic fluid behavior, transport coefficients are sensitive to the underlying microscopic theory. They provide information about the interactions inside the medium. The most frequently studied transport coefficient is the shear viscosity, which is used in viscous hydrodynamic simulations [8]. It has been shown that also the bulk viscosity plays an important role for the time evolution of the QGP [9].

A growing number of studies have examined transport coefficients of the QGP on the basis of effective models at zero or small values of the chemical potential [10–17] where lQCD calculations can serve as a guideline. In order to extend the study of transport coefficients to the part of the phase diagram where the phase transition is possibly changing from a crossover to a first-order one, it is necessary to resort to effective models which describe the chiral phase transition.

The goal of this study is to calculate two transport coefficients of the QGP—the shear viscosity over entropy ratio η/s and the ratio of the electric conductivity to the temperature, σ_0/T —at finite temperature and chemical potential within the framework of an effective relativistic Boltzmann equation in the relaxation-time approximation, where properties of the QGP matter such as the equation-of-state (EoS), the interaction cross sections, and constituent quark masses are described by the extended Polyakov Nambu-Jona-Lasinio (PNJL) model with a critical endpoint (CEP) located at $(T^{CEP}, \mu_q^{CEP}) = (0.11, 0.32)$ GeV [18]. Our study is based on the advances of a previous work [19] where the transport coefficients were calculated within the NJL model at $\mu_B = 0$. However, now we use an advanced Polyakov extension of the NJL model in

*soloveva@itp.uni-frankfurt.de

which the PNJL EoS equals the IQCD EoS at vanishing μ_B ; cf. [18]. Moreover, the framework of the PNJL model allows us to calculate the transport properties near the chiral phase transition at moderate and high μ_B . Here we denote the quark chemical potential as (for the light quarks) $\mu_q = \mu_l = \mu_B/3$ while for the strange quarks we take $\mu_s = 0$.

We compare the PNJL transport coefficients with those from Ref. [20,21], where they were calculated within the dynamical quasiparticle model (DQPM) [22,23] at moderate values of the baryon chemical potential, $\mu_B \leq 0.5$ GeV. Both models are based on rather different ideas: The DQPM is an effective model for the description of nonperturbative (strongly interacting) QCD based on the IQCD EoS. The phase transition there is a crossover for zero as well as for finite μ_B . The degrees of freedom of the DQPM are strongly interacting dynamical quasiparticles—quarks and gluons—with broad spectral functions, whose “thermal” masses and widths increase with growing temperature, while the degrees of freedom of the PNJL are quarks whose masses approach the bare mass when the temperature increases and the chiral condensate disappears. Moreover, in the PNJL the mesonsexist above the Mott transition temperature as resonances. Thus, in the EoS the energy density is shared between the quarks, mesons, and the Polyakov loop potential. We explore how the nature of the degrees of freedom affects the transport properties of the QGP. Moreover, we study the possible influence of the presence of a CEP and of a first-order phase transition at high baryon chemical potential. For the evaluation of the relaxation time we use two different methods: (a) the “averaged transition rate” defined via the thermal averaged quark-quark and quark-antiquark PNJL cross sections and (b) the “weighted” thermal averaged quark-quark and quark-antiquark PNJL cross sections [here by “thermal averaged” cross section we mean the averaging of the interaction cross section over the thermal (anti)quark distribution function]. We discuss the uncertainties related to the theoretical methods based on the relaxation time approximation (RTA).

The paper is organized as follows: In Sec. II we give a brief review of the basic ingredients of the PNJL model, detail the description of the evaluation of the total quark cross sections for different channels, and show the temperature and chemical potential dependence of the total cross sections. In Sec. III we discuss the computation of the specific shear viscosity and the electric conductivity based on the relaxation time approximation of the Boltzmann equation. We consider two methods for the evaluation of the quark relaxation times and discuss differences between them. We compare furthermore our results at $\mu_B = 0$ to calculations from IQCD for $N_f = 0$ for the specific shear viscosity and to IQCD results for $N_f = 2$ and $N_f = 2 + 1$ for the electric conductivity and to predictions of the DQPM for both transport coefficients. In addition, we show the ratio of dimensionless transport coefficients for the full range of chemical potentials. We finalize our study with conclusions in Sec. IV.

II. PNJL QUARK-QUARK CROSS SECTIONS

We start with the calculation of the quark-quark elastic cross sections at finite temperature and chemical potential

TABLE I. Table of the parameters of the PNJL model used in this paper.

m_u (GeV)	m_s (GeV)	G	K	Λ (GeV)
0.005	0.134	$\frac{2.3}{\Lambda^2}$	$\frac{11.0}{\Lambda^5}$	0.569

using scalar and pseudoscalar mesons as exchanged boson within the PNJL model of Ref. [18]. This model is an improved version of the standard Polyakov extended Nambu-Jona-Lasinio model where the pressure is calculated next to leading order in N_c and the effective potential is phenomenologically reparametrized to describe a medium in which also quarks are present. Correspondingly, the masses of the quarks and the mesonic propagators are evaluated using this upgraded PNJL model [18]. We note that the cross sections for quark-meson or quark-diquark channels can also be found in Ref. [24]. They are not used in this study.

A. PNJL model

The PNJL [25–30] model is an extension of the NJL model including thermal gluons on the level of a mean field. The quark-quark interaction remains local, the gluons being only present as an effective potential surrounding the quarks. It can be associated to the $\frac{1}{4}F_{\mu\nu}^a F^{a\mu\nu}$ term in the QCD Lagrangian. The Lagrangian of the PNJL model [26–30] for (color neutral) pseudoscalar and scalar interactions (neglecting the vector and axial-vector vertices for simplicity) is

$$\begin{aligned}
 \mathcal{L}_{PNJL} = & \sum_i \bar{\psi}_i (i\not{D} - m_{0i} + \mu_i \gamma_0) \psi_i \\
 & + G \sum_a \sum_{ijkl} [(\bar{\psi}_i i\gamma_5 \tau_{ij}^a \psi_j) (\bar{\psi}_k i\gamma_5 \tau_{kl}^a \psi_l) \\
 & + (\bar{\psi}_i \tau_{ij}^a \psi_j) (\bar{\psi}_k \tau_{kl}^a \psi_l)] \\
 & - K \det_{ij} [\bar{\psi}_i (\mathbb{I} - \gamma_5) \psi_j] - K \det_{ij} [\bar{\psi}_i (\mathbb{I} + \gamma_5) \psi_j] \\
 & - \mathcal{U}(T; \Phi, \bar{\Phi}).
 \end{aligned} \tag{1}$$

Here $i, j, k, l = 1, 2, 3$ are the flavor indices and τ^a ($a = 1, \dots, 8$) are the $N_f = 3$ flavor generators with the normalization

$$\text{tr}_f (\tau^a \tau^b) = 2\delta^{ab}, \tag{2}$$

with tr_f denoting the trace in the flavor space. m_{0i} stands for the bare quark masses and μ_i for their chemical potential. The covariant derivative in the Polyakov gauge reads $D^\mu = \partial^\mu - i\delta^{\mu 0} A^0$, with $A^0 = -iA_4$ being the temporal component of the gluon field in Euclidean space (we denote $A^\mu = g_s A_a^\mu T_a$). The coupling constant for the scalar and pseudoscalar interaction G is taken as a free parameter (fixed, e.g., by the pion mass in vacuum). The values of the free parameters of the PNJL are displayed in Table I.

The third term of Eq. (1) is the so-called 't Hooft Lagrangian which makes the mass splitting between the η and the η' mesons known as the axial U(1) anomaly. K is a coupling constant (fixed by the value of $m_{\eta'} - m_\eta$) and \mathbb{I} is the identity matrix in Dirac space.

TABLE II. Table of the parameters of the effective potential $U(\phi, \bar{\phi}, T)$ used in this paper.

a_0	a_1	a_2	a_3	b_3	b_4	a	b	c	d	e
6.75	-1.95	2.625	-7.44	0.75	7.5	0.082	0.36	0.72	-1.6	-0.0002

Finally, $\mathcal{U}(T, \Phi, \bar{\Phi})$ is the so-called Polyakov-loop effective potential used to account for the static gluonic contributions to the pressure. The Polyakov line and the Polyakov loop are, respectively, defined as

$$L(\mathbf{x}) = \mathcal{P} \exp \left(i \int_0^{1/T} d\tau A_4(\tau, \mathbf{x}) \right) \quad (3)$$

and

$$\Phi(\mathbf{x}) = \frac{1}{N_c} \text{tr}_c L(\mathbf{x}), \quad (4)$$

where \mathcal{P} is the path-integral ordering operator, and the trace tr_c is taken in the color space.

The value of the potential for the expectation values $\langle \Phi \rangle(T)$, $\langle \bar{\Phi} \rangle(T)$, $\mathcal{U}(T, \langle \Phi \rangle(T), \langle \bar{\Phi} \rangle(T))$, gives up to a minus sign the pressure of the gluons in Yang-Mills (YM) theory, corresponding to QCD for infinitely heavy quarks. The comparison with lattice gauge calculations for pure YM serves therefore as a guideline for the parametrization of the effective potential $U(T)$:

$$-P(T) = \mathcal{U}(T, \langle \Phi \rangle(T), \langle \bar{\Phi} \rangle(T)). \quad (5)$$

The effective potential $U(T, \phi = \langle \Phi \rangle(T), \bar{\phi} = \langle \bar{\Phi} \rangle(T))$ is parametrized following Ref. [18]:

$$\frac{U(\phi, \bar{\phi}, T)}{T^4} = -\frac{b_2(T)}{2} \bar{\phi} \phi - \frac{b_3}{6} (\bar{\phi}^3 + \phi^3) + \frac{b_4}{4} (\bar{\phi} \phi)^2 \quad (6)$$

with the parameters

$$b_2(T) = a_0 + \frac{a_1}{1 + \tau} + \frac{a_2}{(1 + \tau)^2} + \frac{a_3}{(1 + \tau)^3}, \quad (7)$$

where

$$t_{\text{phen}} = 0.57 \frac{T - T_{\text{phen}}(T)}{T_{\text{phen}}(T)} \quad (8)$$

and

$$T_{\text{phen}}(T) = a + bT + cT^2 + dT^3 + e \frac{1}{T}. \quad (9)$$

All the coefficients of the parametrization are listed in Table II.

B. Quarks and mesons in the PNJL

In order to calculate cross sections, the masses of the quarks and the propagators of the exchanged mesons have to be known. The mass of the quarks is determined by solving the traditional gap equations [29] together with a minimisation of the grand potential Ω_{PNJL} with respect to the Polyakov loop expectation value ϕ and $\bar{\phi}$:

$$\begin{aligned} \frac{\partial \Omega_{PNJL}}{\partial \phi} = 0, \quad \frac{\partial \Omega_{PNJL}}{\partial \bar{\phi}} = 0, \\ m_q = m_{q0} - 4G \langle \bar{\psi}_q \psi_q \rangle + 2K \langle \bar{\psi}_q \psi_q \rangle \langle \bar{\psi}_s \psi_s \rangle, \\ m_s = m_{s0} - 4G \langle \bar{\psi}_s \psi_s \rangle + 2K \langle \bar{\psi}_q \psi_q \rangle \langle \bar{\psi}_q \psi_q \rangle, \end{aligned} \quad (10)$$

where

$$\begin{aligned} \Omega_{PNJL}(T, \mu_i, \Phi, \bar{\Phi}) \\ = 2G \sum_i \langle \bar{\psi}_i \psi_i \rangle^2 - 4K \prod_i \langle \bar{\psi}_i \psi_i \rangle - 2N_c \sum_i \int \frac{d^3k}{(2\pi)^3} E_i \\ - 2TN_c \sum_i \int \frac{d^3k}{(2\pi)^3} \left(\frac{1}{N_c} \log[1 + 3(\Phi + \bar{\Phi}) \right. \\ \times e^{-(E_i - \mu_i)/T} e^{-(E_i - \mu_i)/T}] + \frac{1}{N_c} \log[1 + 3(\bar{\Phi} \\ \left. + \Phi e^{-(E_i + \mu_i)/T} e^{-(E_i + \mu_i)/T}) \right] + U_{PNJL}, \end{aligned} \quad (11)$$

with $E_i = \sqrt{k^2 + m_i^2}$.

Figure 1 shows the masses of the u and s quarks as a function of the chemical potential μ_q and the temperature. One can see that a smooth crossover occurs for small chemical potentials. The chiral condensate $\langle \bar{\psi} \psi \rangle$ goes from its maximal value in the hadronic phase down to zero in the QGP phase. At low temperature, this transition is discontinuous and a first-order phase transition occurs that ends with a critical endpoint (CEP) at $\mu_q = 0.320$ GeV, $T = 0.110$ GeV.

The propagators of the mesons are build by resummation of the quark-antiquark loops, leading to the amplitude [31]

$$\mathcal{D} = \frac{2ig_m}{1 - 2g_m \Pi_{ff'}^\pm(k_0, \vec{k})}, \quad (12)$$

where g_m is the coupling constant [32] and $\Pi_{ff'}^\pm(k_0, \vec{k})$ is the polarization function given by

$$\begin{aligned} \Pi_{ff'}^\pm(k_0, \vec{k}) = -\frac{N_c}{4\pi^2} [A_0(m_f, \mu_f, T, \Lambda) + A_0(m_{f'}, \mu_{f'}, T, \Lambda) \\ + [(m_f \pm m_{f'})^2 - (k_0 + \mu_f - \mu_{f'})^2 + \vec{k}^2] \\ \times B_0(\vec{k}, m, \mu, m', \mu', k_0, T, \Lambda)], \end{aligned} \quad (13)$$

where “+” stands for the scalar and “-” for the pseudoscalar mesons.

The one-fermion loop A_0 is separated into a vacuum part and a thermal part, the latter being integrated up to infinity:

$$\begin{aligned} A_0(m_f, \mu_f, T, \Lambda) \\ = -4 \left(\int_0^\infty dp \frac{p^2}{E_f} [-f_f(E_f, T, \mu_f) - f_{\bar{f}}(E_f, T, \mu_f)] \right. \\ \left. + \int_0^\Lambda \frac{p^2 dp}{E_f} \right), \end{aligned} \quad (14)$$

where $E_f = \sqrt{p^2 + m_f^2}$ and the Fermi-Dirac distribution functions $f_{f(\bar{f})}(E_f, T, \mu_f)$ are defined as

$$f_{f(\bar{f})}(E_f, T, \mu_f) = \frac{1}{e^{(E_f \pm \mu_f)/T} + 1}. \quad (15)$$

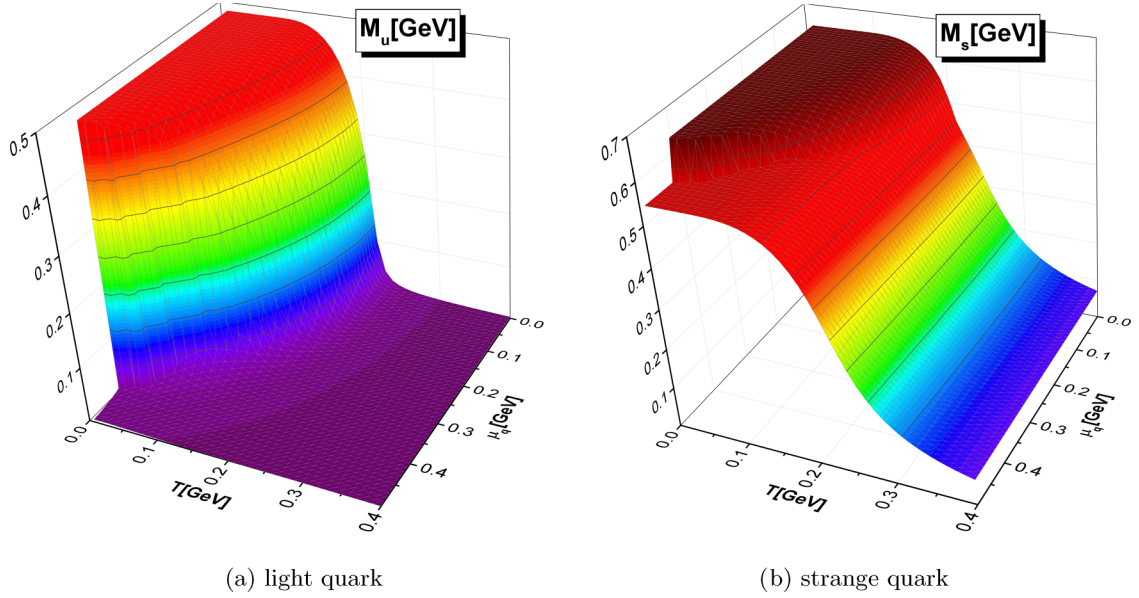


FIG. 1. The masses of light (left) and strange (right) quarks as a function of temperature T and quark chemical potential μ_q calculated within the PNJL model.

The two-Fermion loop B_0 is defined as [33]

$$\begin{aligned}
 B_0(\vec{p}, m_f, \mu_f, m_{f'}, \mu_{f'}, i\nu_m, T, \Lambda) \\
 = 16\pi^2 T \sum_n \exp(i\omega_n \eta) \int_{|q| < \Lambda} \frac{d^3 q}{(2\pi)^3} \\
 \times \frac{1}{[(i\omega_n + \mu_f)^2 - E_f^2]} \frac{1}{[(i\omega_n - i\nu_m + \mu_{f'})^2 - E_{f'}^2]}, \quad (16)
 \end{aligned}$$

with $E_f = \sqrt{\vec{q}^2 + m_f^2}$, $E_{f'} = \sqrt{(\vec{q} - \vec{p})^2 + m_{f'}^2}$. The details of the calculations of B_0 can be found in Ref. [33].

We have $g_m^\pm = G \pm \frac{1}{2}KS^s$ for the pion (+) and its scalar partner (-) and $g_m^\pm = G \pm \frac{1}{2}KS^u$ for the kaon (+) and its scalar partner (-). For the η mesons, the propagators are more complicated because of the mixing terms [31,34]:

$$\mathcal{D} = 2 \frac{\det K}{M_{00}M_{88} - M_{08}^2} \begin{pmatrix} M_{00} & M_{08} \\ M_{80} & M_{88} \end{pmatrix}, \quad (17)$$

$$\begin{aligned}
 \mathcal{D} = \frac{4}{3} \frac{\det K}{M_{00}M_{88} - M_{08}^2} & (M_{00}\bar{\psi}\lambda_0\psi \cdot \bar{\psi}'\lambda_0\psi' \\
 + M_{08}\bar{\psi}\lambda_0\psi \cdot \bar{\psi}'\lambda_8\psi' & + M_{80}\bar{\psi}\lambda_8\psi \cdot \bar{\psi}'\lambda_0\psi' \\
 + M_{88}\bar{\psi}\lambda_8\psi \cdot \bar{\psi}'\lambda_8\psi') & \quad (18)
 \end{aligned}$$

with

$$M_{00} = K_0^+ - \frac{4}{3} \det K (\Pi_{u\bar{u}} + 2\Pi_{s\bar{s}}), \quad (19)$$

$$M_{08} = K_{08}^+ - \frac{4}{3} \sqrt{2} \det K (\Pi_{u\bar{u}} - \Pi_{s\bar{s}}), \quad (20)$$

$$M_{88} = K_8^+ - \frac{4}{3} \det K (2\Pi_{u\bar{u}} + \Pi_{s\bar{s}}), \quad (21)$$

$$\det K = K_0^+ K_8^+ - K_{08}^2, \quad (22)$$

and

$$K_0^\pm = G \mp \frac{1}{3}K(2G^u + G^s), \quad (23)$$

$$K_{08}^\pm = \pm \frac{1}{6}\sqrt{2}K(G^u - G^s), \quad (24)$$

$$K_8^\pm = G \pm \frac{1}{6}K(4G^u - G^s), \quad (25)$$

where G^i is the spinor trace of the propagator $S^i(x, x)$:

$$G^i = N_C i \text{Tr}[S^i(x, x)] = -\frac{N_C}{4\pi^2} m_i A_0(m_i, \mu_i, T, \Lambda). \quad (26)$$

The masses of the pseudoscalar mesons (pion, eta, kaon) at $\mu_q = 0$ are presented in Fig. 2. The doubled quark masses $2m_q$ and $m_q + m_s$ are shown for comparison, too. While in PNJL

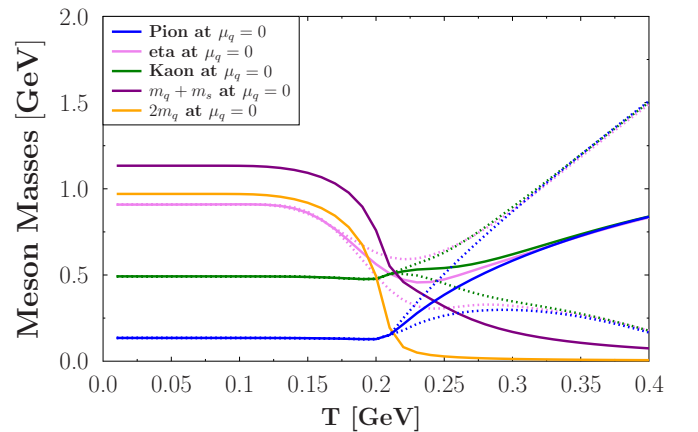


FIG. 2. The PNJL results for the temperature dependence of the meson masses (pion, eta, kaon) as well as double quark masses $2m_q$ and $m_s + m_q$ for $\mu_q = 0$. The dotted lines indicate the $m_{pole} \pm \Gamma$, where the Γ is the imaginary part of the complex pole of the meson propagators and m_{pole} is its real part, indicated by solid lines.

the quark masses drop with increasing temperature to their bare values due to the disappearance of the chiral condensate in the vicinity of the phase transition, the meson masses increase with temperature. In PNJL mesons become unstable above the Mott temperature, $T > T_{M\pi}$, where the total mass of the constituent quarks equals the meson mass. Above $T_{M\pi}$ the mesons can decay into a $q\bar{q}$ pair. Therefore the pole of the meson propagator becomes complex above $T_{M\pi}$. The dotted lines in Fig. 2 indicate $m_{pole} \pm \Gamma$, where Γ is the imaginary part of the complex pole of the meson propagator (which could be associated to the decay width) and m_{pole} is its real part, indicated by solid lines. In contrast to mesons, the quarks in the PNJL stay on shell.

C. The PNJL equation of state

The equation of state is needed to evaluate the entropy density, necessary to determine the shear viscosity to entropy ratio. Here we present the equation of state of the improved PNJL model advanced in [18] which matches the lattice results of Ref. [35]. The improved PNJL model differs from the standard PNJL model in two aspects:

- (i) The grand potential includes next to leading order contributions in N_c and contains therefore contributions from mesons.
- (ii) There is a temperature dependent rescaling of the T_0 parameters of the standard Polyakov effective potential—see Eq. (11) and Table II—in order to phenomenologically reproduce the quark gluon interactions in the medium.

In next-to-leading order the grand potential contains an additional term, Ω_M , caused by the diagrams of the order $O(N_c = 1)$ in the N_c expansion. This term is given by [18,36]

$$\Omega_M = -\frac{g_M}{8\pi^3} \int dpp^2 \int \frac{ds}{\sqrt{s + \vec{k}^2}} \times \left[\frac{1}{\exp[(\sqrt{s + \vec{k}^2} - \mu)/T - 1]} + \frac{1}{\exp[(\sqrt{s + \vec{k}^2} + \mu)/T - 1]} \right] \delta(\sqrt{s}, T, \mu_M). \quad (27)$$

Here g_M is the degeneracy of the meson and $\delta(\sqrt{s}, T, \mu_M)$ is the phase shift defined by

$$\delta(\sqrt{s}, T, \mu_M) = -\text{Arg}[1 - 2K\Pi(\omega - \mu_M + i\epsilon, \vec{k})], \quad (28)$$

where Π is the polarization function of the meson. Ω_M represents a mesonic pressure that dominates at low temperature and is non-negligible around T_C , as seen Fig. 3. As Fig. 4 shows, this equation of state reproduces the lattice results of Ref. [35] for vanishing chemical potential. Also for large chemical potentials and low temperatures, a region which is accessible for pQCD calculations, we reproduce the pQCD calculations of [37] as shown in Fig. 5.

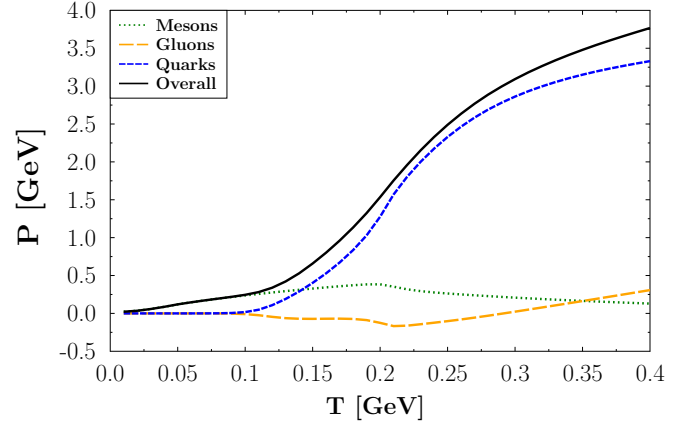


FIG. 3. Meson, gluon, and quark contributions to the total pressure as well as the total pressure (solid black line) at $\mu_q = 0$ as a function of the temperature.

D. Quark-quark scattering in the PNJL

There are two possible Feynman diagrams for quark-quark scattering: the t and u channels as indicated in Fig. 6. The associated squares of the matrix elements for the t and u channels and their interference term are defined as

$$\frac{1}{4N_C^2} \sum_{s,c} |M_{u}|^2 = |\mathcal{D}_u^S|^2 u_{14}^+ u_{23}^+ + |\mathcal{D}_u^P|^2 u_{14}^- u_{23}^-, \quad (29)$$

$$\begin{aligned} \frac{1}{4N_C^2} \sum_{s,c} |M_{ut}| &= \frac{1}{4N_C} [\mathcal{D}_t^S \mathcal{D}_u^{S*} (t_{13}^+ t_{24}^+ - s_{12}^+ s_{34}^+ + u_{14}^+ u_{23}^+) \\ &\quad - \mathcal{D}_t^S \mathcal{D}_u^{P*} (t_{13}^+ t_{24}^+ - s_{12}^- s_{34}^- + u_{14}^- u_{23}^-) \\ &\quad - \mathcal{D}_t^P \mathcal{D}_u^{S*} (t_{13}^- t_{24}^- - s_{12}^- s_{34}^- + u_{14}^- u_{23}^-) \\ &\quad + \mathcal{D}_t^P \mathcal{D}_u^{P*} (t_{13}^- t_{24}^- - s_{12}^+ s_{34}^+ + u_{14}^- u_{23}^-)], \quad (30) \end{aligned}$$

$$\frac{1}{4N_C^2} \sum_{s,c} |M_t|^2 = |\mathcal{D}_t^S|^2 t_{13}^+ t_{24}^+ + |\mathcal{D}_t^P|^2 t_{13}^- t_{24}^-. \quad (31)$$

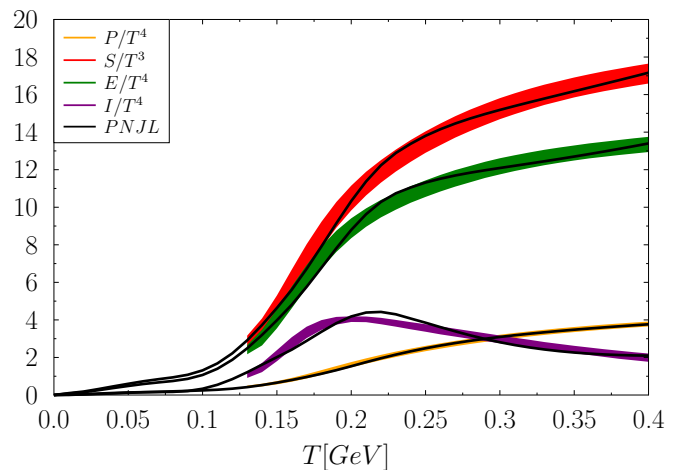


FIG. 4. Pressure, entropy density, energy density, and interaction measure calculated within the PNJL using the sum of Eqs. (11) and (27) for $\mu_q = 0$ (colored lines described in the legend) in comparison to the lattice QCD results [35], indicated as colored bands.

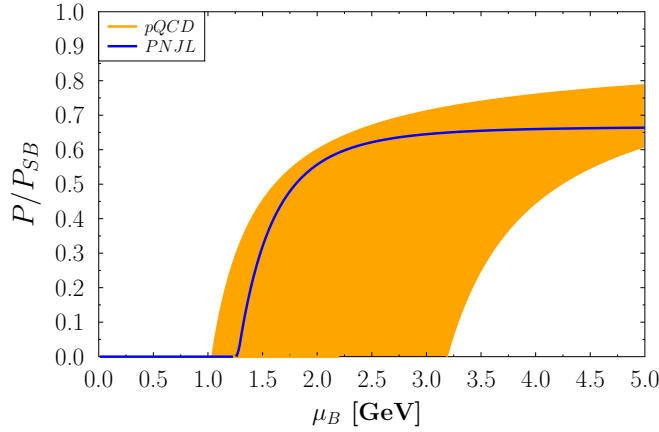


FIG. 5. The quark pressure divided by the pressure in the Stefan-Boltzmann limit as a function of μ_B for a temperature of $T = 0.001$ GeV. We compare pQCD calculations [37] (orange area) with the result of our PNJL approach (blue line).

Here

$$t_{ij}^{\pm} = t - (m_i \pm m_j)^2, \quad (32)$$

$$u_{ij}^{\pm} = u - (m_i \pm m_j)^2, \quad (33)$$

$$s_{ij}^{\pm} = s - (m_i \pm m_j)^2. \quad (34)$$

\mathcal{D}^S and \mathcal{D}^P are the propagators of the exchanged scalar and pseudoscalar meson, respectively,; see Eq. (12).

Table III lists the mesons which can be exchanged in the t and u channels in the different quark-quark cross sections [32].

E. Quark-antiquark scattering in the PNJL

For quark-antiquark scattering only s and t channels are possible. The corresponding diagrams are shown in Fig. 7.

The corresponding squares of the matrix elements for the s and t channels and their interference term are given by

$$\frac{1}{4N_C^2} \sum_{s,c} |M_s|^2 = |\mathcal{D}_s^S|^2 s_{12}^+ s_{34}^+ + |\mathcal{D}_s^P|^2 s_{12}^- s_{34}^-, \quad (35)$$

$$\begin{aligned} \frac{1}{4N_C^2} \sum_{s,c} |M_{st}| &= \frac{1}{4N_C} [\mathcal{D}_s^S \mathcal{D}_t^{S*} (s_{12}^+ s_{34}^+ - u_{14}^+ u_{23}^+ + t_{13}^+ t_{24}^+) \\ &\quad - \mathcal{D}_s^S \mathcal{D}_t^{P*} (s_{12}^+ s_{34}^+ - u_{14}^- u_{24}^- + t_{13}^- t_{24}^-) \\ &\quad - \mathcal{D}_s^P \mathcal{D}_t^{S*} (s_{12}^- s_{34}^- - u_{14}^- u_{23}^- + t_{13}^+ t_{24}^+) \\ &\quad + \mathcal{D}_s^P \mathcal{D}_t^{P*} (s_{12}^- s_{34}^- - u_{14}^+ u_{23}^+ + t_{13}^- t_{24}^-)], \quad (36) \end{aligned}$$

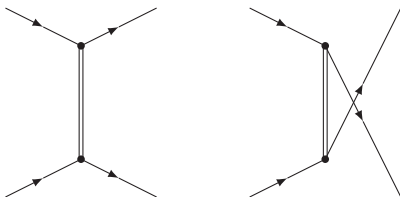


FIG. 6. The Feynman diagrams for the t and u channels which contribute to the quark-quark cross sections.

TABLE III. Mesons which can be exchanged in the t and u channels in the different quark-quark cross sections.

Process	Exchanged mesons in u channel	Exchanged mesons in t channel
$ud \rightarrow ud$	π, σ_π	$\pi, \eta, \eta', \sigma_\pi, \sigma, \sigma'$
$uu \rightarrow uu$	$\pi, \eta, \eta', \sigma_\pi, \sigma, \sigma'$	$\pi, \eta, \eta', \sigma_\pi, \sigma, \sigma'$
$us \rightarrow us$	K, σ_K	$\eta, \eta', \sigma, \sigma'$
$ss \rightarrow ss$	$\eta, \eta', \sigma, \sigma'$	$\eta, \eta', \sigma, \sigma'$

$$\frac{1}{4N_C^2} \sum_{s,c} |M_t|^2 = |\mathcal{D}_t^S|^2 t_{13}^+ t_{24}^+ + |\mathcal{D}_t^P|^2 t_{13}^- t_{24}^-. \quad (37)$$

Table IV presents the mesons which can be exchanged in the s and t channels in the different quark-(anti)quark cross sections [32].

F. Integration boundaries and the total cross sections

The differential cross sections for the quark-quark and quark-antiquark scattering for t, u channels and t, s channels, respectively, are given by the following expressions:

$$\frac{d\sigma}{dt} = \frac{1}{16\pi s_{12}^+ s_{12}^-} \frac{1}{4N_C^2} \sum_{s,c} |\mathcal{M}_{s/uv} - \mathcal{M}_t|^2. \quad (38)$$

The total cross section in a thermal medium is obtained by integration over t :

$$\sigma = \int_{t_-}^{t_+} dt \frac{d\sigma}{dt} [1 - f_F(E_3, T, \mu)][1 - f_F(E_4, T, \mu)], \quad (39)$$

where $1 - f_F$ is the Pauli blocking factor for the fermions due to the fact that some of the final states are already occupied by other quarks (antiquarks). The limits of the integrations are defined as

$$\begin{aligned} t_{\pm} &= m_1^2 + m_3^2 - \frac{1}{2s} (s + m_1^2 - m_2^2)(s + m_3^2 - m_4^2) \\ &\quad \pm 2\sqrt{\frac{(s + m_1^2 - m_2^2)^2}{4s} - m_1^2} \sqrt{\frac{(s + m_3^2 - m_4^2)^2}{4s} - m_3^2}. \quad (40) \end{aligned}$$

where m_1 and m_2 are the masses of the particles in the entrance channel and m_3 and m_4 of those in the exit channel.

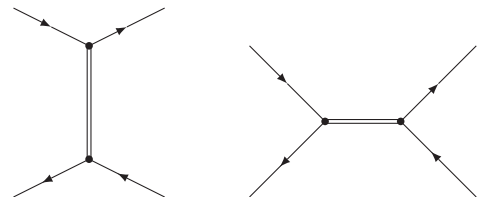


FIG. 7. The Feynman diagrams for the t and s channels which contribute to the quark-antiquark cross sections.

TABLE IV. Mesons which can be exchanged in the s and t channels in the different quark-antiquark cross sections.

Process	Exchanged mesons in s channel	Exchanged mesons in t channel
$u\bar{d} \rightarrow u\bar{d}$	π, σ_π	$\pi, \eta, \eta', \sigma_\pi, \sigma, \sigma'$
$u\bar{u} \rightarrow u\bar{u}$	$\pi, \eta, \eta', \sigma_\pi, \sigma, \sigma'$	$\pi, \eta, \eta', \sigma_\pi, \sigma, \sigma'$
$u\bar{u} \rightarrow d\bar{d}$	$\pi, \eta, \eta', \sigma_\pi, \sigma, \sigma'$	π, σ_π
$u\bar{s} \rightarrow u\bar{s}$	K, σ_K	$\eta, \eta', \sigma, \sigma'$
$u\bar{u} \rightarrow s\bar{s}$	$\eta, \eta', \sigma, \sigma'$	K, σ_K
$s\bar{s} \rightarrow u\bar{u}$	$\eta, \eta', \sigma, \sigma'$	K, σ_K
$s\bar{s} \rightarrow s\bar{s}$	$\eta, \eta', \sigma, \sigma'$	$\eta, \eta', \sigma, \sigma'$

G. Results for elastic cross section

In Fig. 8 we present the quark-quark cross sections for $ud \rightarrow ud$ elastic scattering versus \sqrt{s} at $T = 190$ MeV for different $\mu_q = 0, 0.1, 0.2$ GeV (upper plot) and at $\mu_q = 0$ for different $T = 190, 220,$ and 300 MeV (lower plot). As follows from Fig. 8 these cross sections are rather small and show a smooth behavior versus the center of mass (c.m.) energy. They are decreasing with increasing temperature and chemical

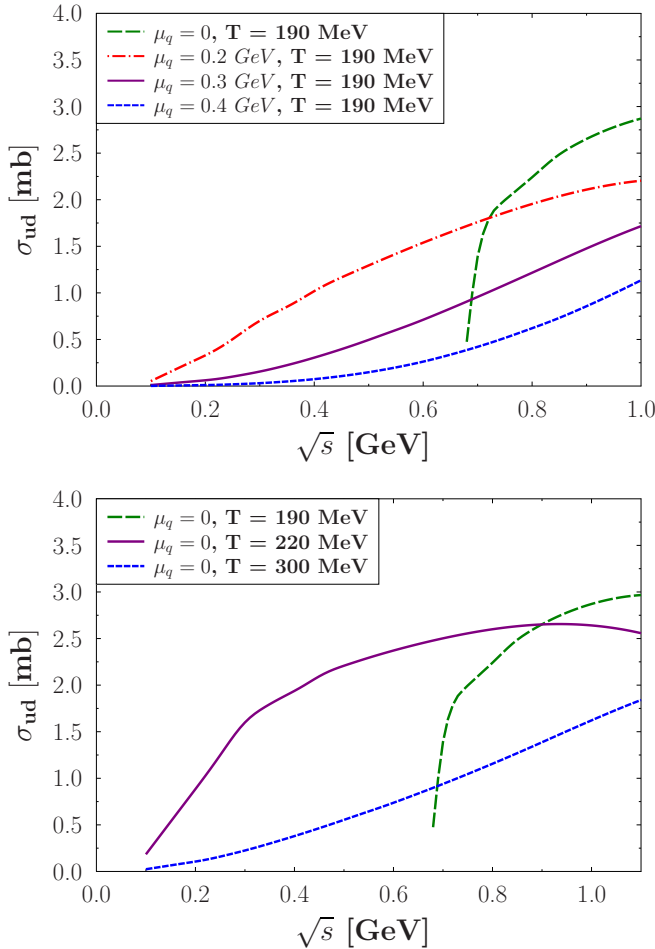


FIG. 8. The cross section σ_{ud} versus \sqrt{s} at $T = 190$ MeV for $\mu_q = 0, 0.1, 0.2$ GeV (upper) and at $\mu_q = 0$ for $T = 190, 220,$ and 300 MeV (lower).

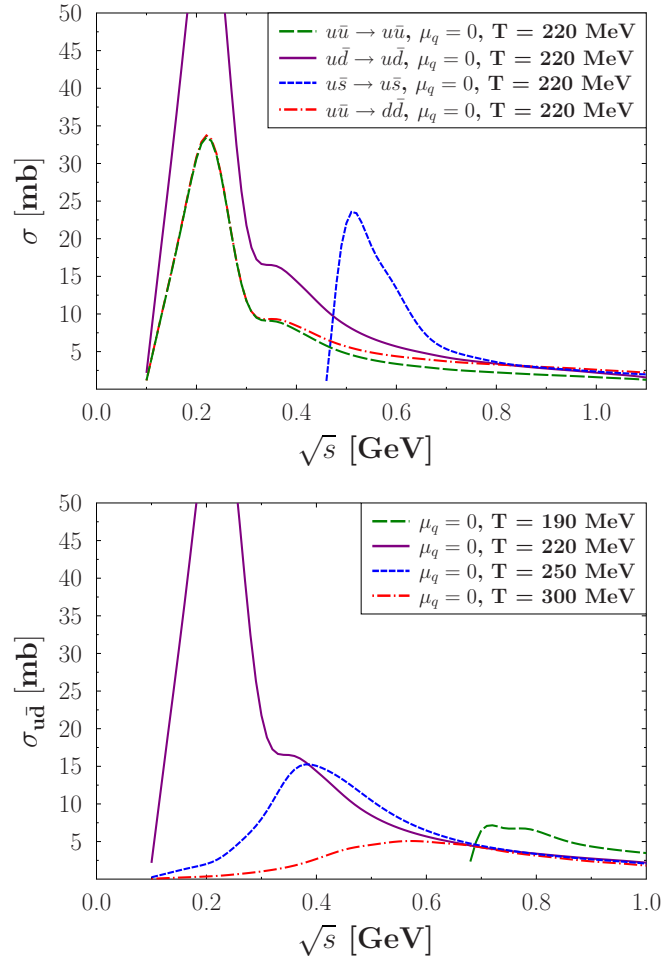


FIG. 9. The resonance behavior of the $u\bar{u} \rightarrow u\bar{u}$, $u\bar{d} \rightarrow u\bar{d}$, $u\bar{u} \rightarrow d\bar{d}$, and $u\bar{s} \rightarrow u\bar{s}$ cross sections versus \sqrt{s} at $T = 220$ GeV and $\mu = 0$ (upper) and at $\mu_q = 0$ for $T = 190, 220, 250$ and 300 MeV.

potential, as expected because the mass of the exchanged meson and its decay width increase with temperature. At low temperature and chemical potential the masses of the quarks are large and tend to vanish at large T and μ_q . Consequently, the threshold, given by $\sqrt{s}_{thr} = \text{Max}(m_{in}^a + m_{in}^b, m_{out}^a + m_{out}^b)$, is high at low μ_q and low T , as one can see from Fig. 8 as well.

The more interesting processes are quark-antiquark collisions. In this case the s channel allows for a resonance of the exchanged meson with the incoming quarks which leads to a large peak in the cross sections.

Figure 9 (upper part) displays the cross section at different channels showing a resonance behavior. The $u\bar{s} \rightarrow u\bar{s}$ resonance is lower than the others because the strange quark is heavier than the u and quarks at $\mu_q = 0$ and $T = 200$ MeV. The other resonances differ only by their flavor factors [38]. The $u\bar{d} \rightarrow u\bar{d}$ channel has the largest factor; $u\bar{u} \rightarrow u\bar{u}$ has a lower factor than $u\bar{u} \rightarrow d\bar{d}$ but allows for a η meson exchange, which is not the case for the $u\bar{u} \rightarrow d\bar{d}$ channel.

The behavior of the $u\bar{d} \rightarrow u\bar{d}$ cross section for different temperatures is displayed in Fig. 9 (lower part). One can see that the resonance is shifted to the right when the

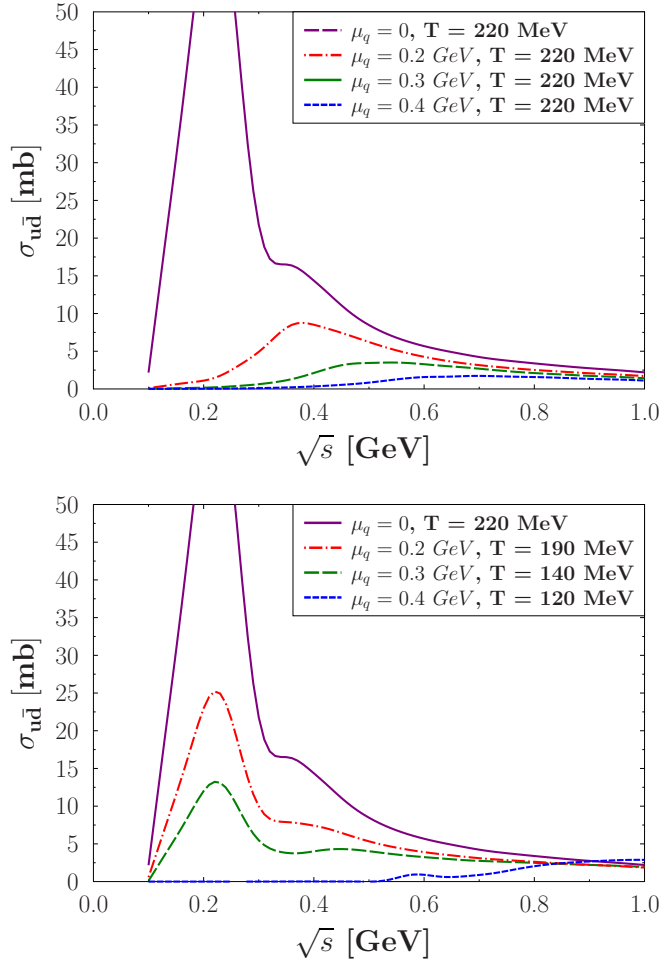


FIG. 10. The resonant $u\bar{d}$ cross section versus \sqrt{s} at $T = 220$ MeV for $\mu_q = 0, 200, 300,$ and 400 MeV (upper) and for different combinations of T, μ_q (lower).

temperature increases. Since the mass of the mesons increases with temperature, the cross section with the pion in the s channel becomes resonant at the corresponding \sqrt{s} . The peak becomes lower with increasing temperature and disappears finally at large temperatures since the decay width of the pion becomes larger with increasing temperature; see Fig. 2. The kinematic threshold forbids any resonance state below the Mott temperature. This explains the flatness of the $u\bar{d} \rightarrow u\bar{d}$ cross section at $T = 190$ MeV.

Figure 10 shows the behavior of the resonance peak with increasing chemical potential. For a given temperature, the mass of the pion becomes larger with increasing chemical potential and the peak is shifted to a smaller value of the temperature. Beyond the critical endpoint $\mu_{CEP} = 0.32$ GeV, the cross section is flat and no resonance behavior shows up anymore.

The calculation of the two cross sections $s\bar{s} \rightarrow u\bar{u}$ and $u\bar{u} \rightarrow s\bar{s}$ can be double checked since they obey detailed balance:

$$\sigma_{cd \rightarrow ij}(s) = \frac{p_{ij}^{2cm}(s)}{p_{cd}^{2cm}(s)} \sigma_{ij \rightarrow cd}(s). \quad (41)$$

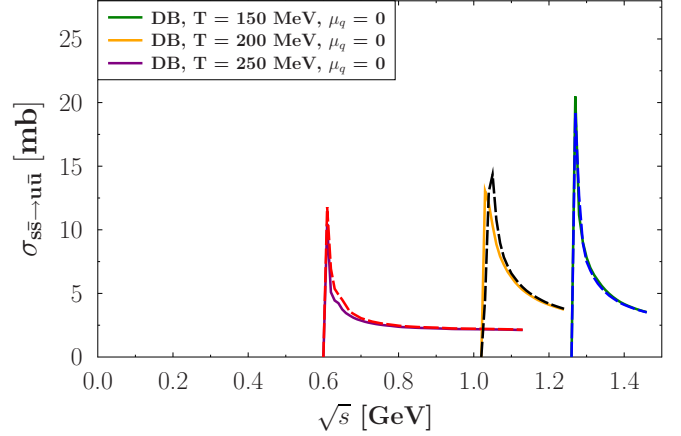


FIG. 11. The cross section for the $s\bar{s} \rightarrow u\bar{u}$ channel calculated by detailed balance (solid lines, DB) for $T = 150, 200, 250$ MeV at $\mu_q = 0$ as compared to the direct numerical calculation (dashed lines).

Figure 11 shows the cross section for the $s\bar{s} \rightarrow u\bar{u}$ channel at $\mu_q = 0$ and $T = 150, 200, 250$ MeV calculated directly (dashed lines) and by detailed balance (41) (solid lines). One can see that the two calculations show a good agreement with each other.

III. TRANSPORT COEFFICIENTS IN THE PNJL MODEL

A. Transport coefficients in the relaxation time approximation

In the relativistic kinetic theory one can determine the transport coefficients with the help of the relaxation time approximation of the Boltzmann equation for the quasiparticles with dynamical masses $M_i(T, \mu_q)$ [39–42]:

$$k_i^\mu \partial_\mu f_i + \frac{1}{2} \partial^\mu M_i^2 \partial_{(k_i, \mu)} f_i = \sum_{j=1}^{N_{\text{species}}} C_{ij}(x, k), \quad (42)$$

where $C_{ij}(x, k)$ is the two-body collision term which contains only quasielastic $2 \leftrightarrow 2$ scatterings, while the second term contains $F_i^\mu = \partial^\mu M_i$ and is an external force attributed to the residual mean field interaction due to the medium dependent effective masses $M_i(T, \mu_q)$.

In order to evaluate transport coefficients we consider a small departure from equilibrium, where the distribution function can be expressed as

$$\begin{aligned} f_i(x, k, t) &= f_i^{(0)}(x, k, t) + f_i^{(1)}(x, k, t) \\ &= f_i^{(0)}(x, k, t)[1 + \delta f_i(x, k, t)]. \end{aligned} \quad (43)$$

$f_i^{(0)}(x, k, t)$ is the local equilibrium distribution function and $f_i^{(1)}(x, k, t)$ contains $\delta f_i(x, k, t)$, which is the nonequilibrium part to first order in gradients. Quark systems in equilibrium can be described by the Fermi-Dirac distribution function:

$$f_i^{(0)}(E_i, T, \mu_q) = \frac{1}{e^{(E_i \pm \mu_q)/T} + 1}, \quad (44)$$

where $E_i = \sqrt{p_i^2 + m_i^2}$ is the on-shell quark energy, T is the temperature, and $\mu_q = \mu_B/3$ for the light quarks, $\mu_s = 0$ for

the strange quark. The (anti)quark density is defined as

$$n_i(T, \mu_q) = d_q \int \frac{d^3 p}{(2\pi)^3} f_i^{(0)}, \quad (45)$$

where $i = u, d, s, \bar{u}, \bar{d}, \bar{s}$ and $d_q = 2 \times N_c$ is degeneracy factor for (anti)quarks.

In order to take into account the Polyakov loop contributions we use the modified Fermi-Dirac distribution:

$$f_i^\phi = \frac{\phi e^{-(E_i \mp \mu)/T} + 2\bar{\phi} e^{-2(E_i \mp \mu)/T} + e^{-3(E_i \mp \mu)/T}}{1 + 3\phi e^{-(E_i \mp \mu)/T} + 3\bar{\phi} e^{-2(E_i \mp \mu)/T} + e^{-3(E_i \mp \mu)/T}}, \quad (46)$$

where $i = q, \bar{q}$. The minus sign refers to quarks ($i = q$), while the plus sign refers to antiquarks ($i = \bar{q}$). For antiquarks we have to exchange ϕ and $\bar{\phi}$.

In the QGP phase the modified distributions approach the standard Fermi-Dirac distributions for $\phi \rightarrow 1$, while in the hadronic phase, for $\phi \rightarrow 0$, we get distributions with three times the quark energy in the exponent, which can be interpreted as a Fermi-Dirac distribution function of a particle with three times the quark mass.

In the relaxation time approximation to first order in the deviation from equilibrium the collision term is given by [43]

$$\sum_{j=1}^{N_{\text{species}}} C_{ij}^{(1)}[f_i] = -\frac{E_i}{\tau_i} (f_i - f_i^{(0)}) = -\frac{E_i}{\tau_i} f_i^{(1)} + O(\text{Kn}^2), \quad (47)$$

where τ_i is the relaxation time in the heat bath rest system for the particle species i , $\text{Kn} \sim l_{\text{micro}}/L_{\text{macro}}$ is the Knudsen number which denotes the ratio between the relevant

microscopic/transport length scales. l_{micro} is in our case the mean free path λ , and the macroscopic scale L_{macro} is the characteristic length of the system.

B. Quark relaxation time

The RTA is often used in the framework of effective models for the estimation of transport coefficients in the QGP phase. It is worth noting that the results of transport calculations depend not only on the EoS, which can be fitted to the IQCD results, but also (if no local equilibrium is assumed) on transport coefficients and therefore on the method of how to evaluate quark and gluon relaxation times.

In this section we apply two different approaches for the calculation of the quark relaxation time, which are commonly used in the literature: (1) the so-called ‘‘averaged transition rate’’ defined via the thermal averaged quark-quark and quark-antiquark PNJL cross sections and (2) the ‘‘weighted’’ thermal averaged quark-quark and quark-antiquark PNJL cross sections. As will be demonstrated later, the differences between the two methods are quite essential and influence substantially the final results for the transport coefficients.

1. Method 1 for the quark relaxation time

We start with the estimation of the quark relaxation time through the averaged interaction rate, related to the thermal averaged quark-quark and quark-antiquark PNJL cross sections, advanced in [40,42,44,45]. The momentum dependent relaxation time can be expressed through the on-shell interaction rate in the medium rest system where the incoming quark has a four-momentum $P_i = (E_i, \mathbf{p}_i)$:

$$\begin{aligned} \tau_i^{-1}(p_i, T, \mu_q) &= \Gamma_i(p_i, T, \mu_q) \\ &= \frac{1}{2E_i} \sum_{j=q,\bar{q}} \frac{1}{1 + \delta_{cd}} \int \frac{d^3 p_j}{(2\pi)^3 2E_j} d_q f_j^{(0)}(E_j, T, \mu_q) \int \frac{d^3 p_c}{(2\pi)^3 2E_c} \int \frac{d^3 p_d}{(2\pi)^3 2E_d} |\bar{\mathcal{M}}|^2(p_i, p_j, p_c, p_d) \\ &\quad \times (2\pi)^4 \delta^{(4)}(p_i + p_j - p_c - p_d) (1 - f_c^{(0)}) (1 - f_d^{(0)}) \\ &= \frac{1}{2E_i} \sum_{j=q,\bar{q}} \frac{1}{1 + \delta_{cd}} \int \frac{d^3 p_j}{(2\pi)^3 2E_j} d_q f_j^{(0)}(E_j, T, \mu_q) \frac{1}{16\pi \sqrt{s}} \frac{1}{p_{cm}} \int dt |\bar{\mathcal{M}}|^2(s, t) (1 - f_c^{(0)}) (1 - f_d^{(0)}) \\ &= \sum_{j=q,\bar{q}} \int \frac{d^3 p_j}{(2\pi)^3} d_q f_j^{(0)}(E_j, T, \mu_q) v_{\text{rel}} \sigma_{ij \rightarrow cd}(s, T, \mu_q). \end{aligned} \quad (48)$$

The indices i and j refer to particles in the entrance channel, c and d to those in the exit channel. $f_i^{(0)}$ is the modified Fermi-Dirac distribution function taking into account the Polyakov loop [Eq. (46)]. $|\bar{\mathcal{M}}|^2$ denotes the matrix element squared averaged over the color and spin of the incoming partons, and summed over those of the final partons. \sqrt{s} can be conveniently calculated from the four-vectors of the incoming partons. The cross section without the Pauli blocking factors is

$$\sigma(\sqrt{s}) = \int dt \frac{1}{64\pi s p_{cm}^2} |\bar{\mathcal{M}}|^2. \quad (49)$$

The relative velocity in the c.m. frame is given by

$$v_{\text{rel}} = \frac{\sqrt{(p_i \cdot p_j)^2 - m_i^2 m_j^2}}{E_i E_j} = \frac{p_{cm} \sqrt{s}}{E_i E_j}. \quad (50)$$

p_{cm} is the momenta of the initial (i, j) as well as of the final quarks (c, d) in the c.m. frame given by

$$p_{cm} = \frac{\sqrt{[s - (m_{i,c} - m_{j,d})^2][s - (m_{i,c} + m_{j,d})^2]}}{2\sqrt{s}}. \quad (51)$$

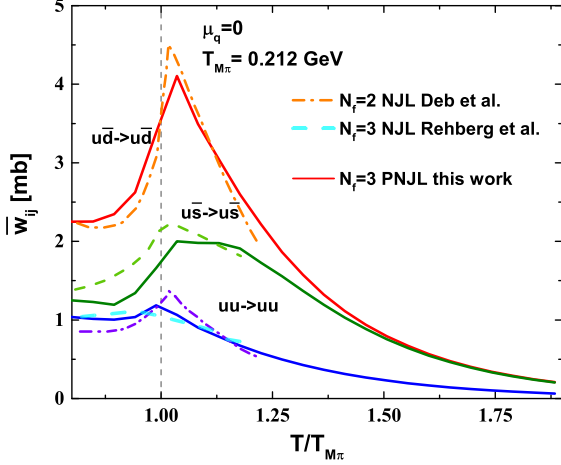


FIG. 12. Energy averaged transition rates $\bar{w}_{ij}(T, \mu_q)$ for different quark-quark(antiquark) scattering processes [$u\bar{d} \rightarrow u\bar{d}$ (red and orange lines), $u\bar{s} \rightarrow u\bar{s}$ (green lines), $uu \rightarrow uu$ (blue, cyan, and violet lines)] as a function of scaled temperature $T/T_{M\pi}$ for $\mu_q = 0$. The solid lines corresponds to the actual results from Eq. (53). Green and cyan dashed lines correspond to the results from Ref. [32]. Orange and violet dash-dotted lines correspond to the estimations from Ref. [46].

The averaged relaxation time can be obtained from the relaxation time of Eq. (48) by averaging over p_i

$$\tau_i^{-1}(T, \mu_q) = \frac{1}{n_i(T, \mu_q)} \int \frac{d^3 p_i}{(2\pi)^3} d_q f_i^{(0)} \tau_i^{-1}(p_i, T, \mu_q). \quad (52)$$

The relaxation time can be expressed via the averaged transition rate \bar{w}_{ij} defined as

$$\bar{w}_{ij} = \frac{1}{n_i n_j} \int \frac{d^3 p_i}{(2\pi)^3} \int \frac{d^3 p_j}{(2\pi)^3} d_q f_i^{(0)}(E_i, T, \mu_q) d_q \times f_j^{(0)}(E_j, T, \mu_q) \cdot v_{\text{rel}} \sigma_{ij \rightarrow cd}(s, T, \mu_q). \quad (53)$$

We note that, in spite of \bar{w}_{ij} being called in the literature ‘‘averaged transition rate,’’ it has the dimension of a cross section. Using \bar{w}_{ij} defined by Eq. (53), the average quark relaxation time is given by [32]

$$\tau_i^{-1}(T, \mu_q) = \sum_{j=q, \bar{q}} n_j(T, \mu_q) \bar{w}_{ij} \quad (54)$$

Figure 12 illustrates the results of the energy averaged transition rates $\bar{w}_{ij}(T, \mu_q)$ for three scattering processes: $u\bar{d} \rightarrow u\bar{d}$ (red and orange lines), $u\bar{s} \rightarrow u\bar{s}$ (green lines), $uu \rightarrow uu$ (blue, cyan, and violet lines) as a function of scaled temperature $T/T_{M\pi}$ (where $T_{M\pi}$ is the Mott temperature) for $\mu_q = 0$ from Eq. (53) in comparison to the previous NJL results taken from Ref. [32] (green and cyan dashed lines, $N_f = 3$) and Ref. [46] (orange and violet dash-dotted lines, $N_f = 2$). Our results are in a good agreement with these NJL results; a small difference arises due to different parameters of the models and different quark masses. Momentum averaged transition rates $\bar{w}_{ij}(T, \mu_q)$ for qq (solid lines) and $q\bar{q}$ (dashed lines) scattering channels are presented in Fig. 13 as a function of scaled

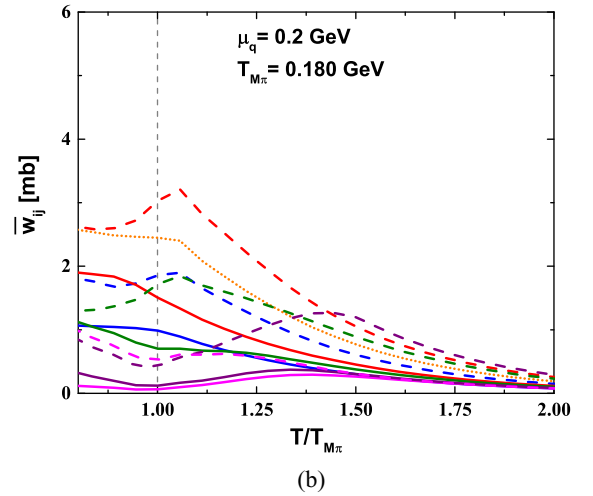
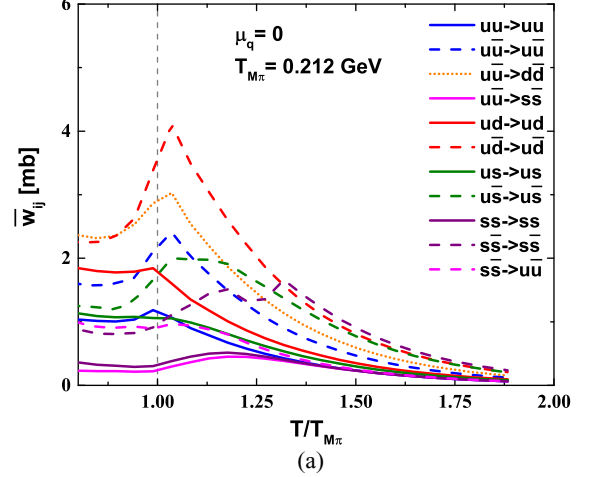


FIG. 13. Energy averaged transition rates $\bar{w}_{ij}(T, \mu_q)$ for different quark-quark(antiquark) scattering processes as a function of scaled temperature $T/T_{M\pi}$ for (a) $\mu_q = 0$ (upper) and (b) $\mu_q = 0.2$ GeV (lower). The solid and dashed lines correspond to the actual results from Eq. (53) for the quark-quark and the quark-antiquark scatterings.

temperature $T/T_{M\pi}$ for (a) $\mu_q = 0$ and (b) $\mu_q = 0.2$ GeV. Near $T_{M\pi}$ the rates $\bar{w}_{ij}(T, \mu_q)$ have a peak, which is followed by a decrease with increasing temperature. While the values of the $q\bar{q}$ rates $\bar{w}_{q\bar{q}}(T, \mu_q)$ are higher than those of the qq channels, the antiquark densities are smaller than the quark densities at nonzero μ_q (see Fig. 14).

2. Method 2 for the quark relaxation time

We continue the estimation of quark relaxation times with an approach which was introduced by Zhuang [25] for the calculation of the mean free path and then modified by Sasaki [47] for the evaluation of the relaxation time. It is based on the ‘‘weighted’’ thermal averaged quark-quark and quark-antiquark PNJL cross sections. In the dilute gas approximation the relaxation time for the species i is defined in [47] as

$$\tau_i^{-1}(T, \mu_q) = \sum_{j=q, \bar{q}} n_j(T, \mu_q) \bar{\sigma}_{ij}(T, \mu_q). \quad (55)$$

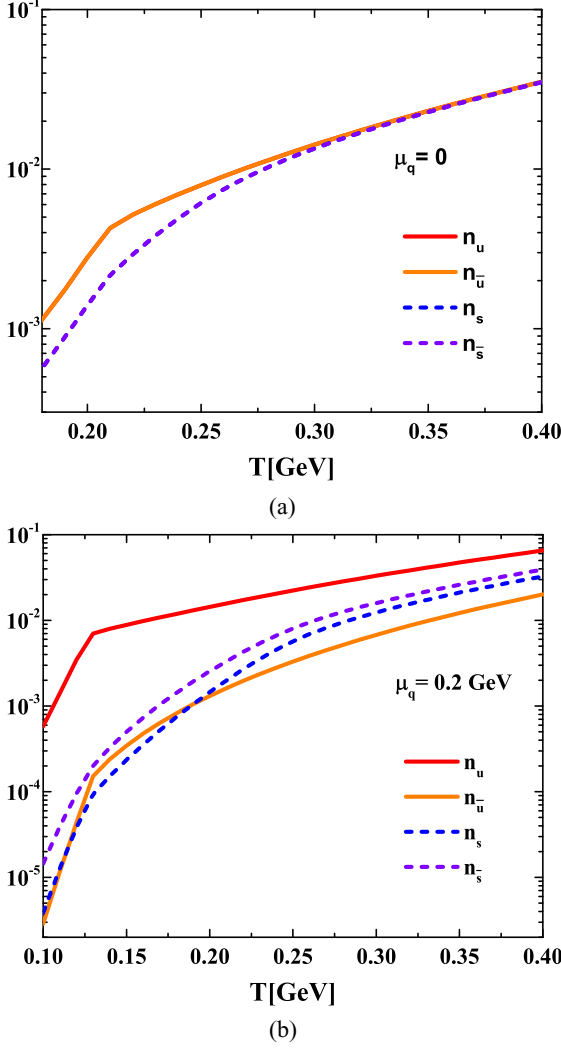


FIG. 14. Light and strange quarks (antiquarks) densities $n_i(T, \mu_q)$ with f_i^ϕ -modified Fermi distributions from Eq. (46) as a function of temperature for (a) $\mu_q = 0$ (upper) and (b) $\mu_q = 0.2$ GeV (lower). The solid orange and red lines correspond to the light quark and antiquark densities, while the dashed blue and violet lines correspond to the strange quark and antiquark densities.

$\bar{\sigma}_{ij}(T, \mu_q)$ is the “weighted” thermal averaged total PNJL scattering cross section,

$$\bar{\sigma}_{ij}(T, \mu_q) = \int_{s_0}^{s_{\max}} ds \sigma_{ij \rightarrow cd}(T, \mu_q, s) P(T, \mu_q, s),$$

$$P(T, \mu_q, s) = C' \int d^3 p_i d^3 p_j d_q f_i^{(0)}(E_i, T, \mu_q) d_q$$

$$\times f_j^{(0)}(E_j, T, \mu_q) \delta[\sqrt{s} - (E_i + E_j)]$$

$$\times \delta^3(\vec{p}_i + \vec{p}_j) v_{\text{rel}}. \quad (56)$$

Here $P(T, \mu_q, s)$ is the probability of finding a quark-antiquark or quark-quark pair with a center-of-mass energy \sqrt{s} and a zero total momentum. $P(T, \mu_q, s)$ is normalized as

$$\int_{s_0}^{s_{\max}} ds P(T, \mu_q, s) = 1. \quad (57)$$

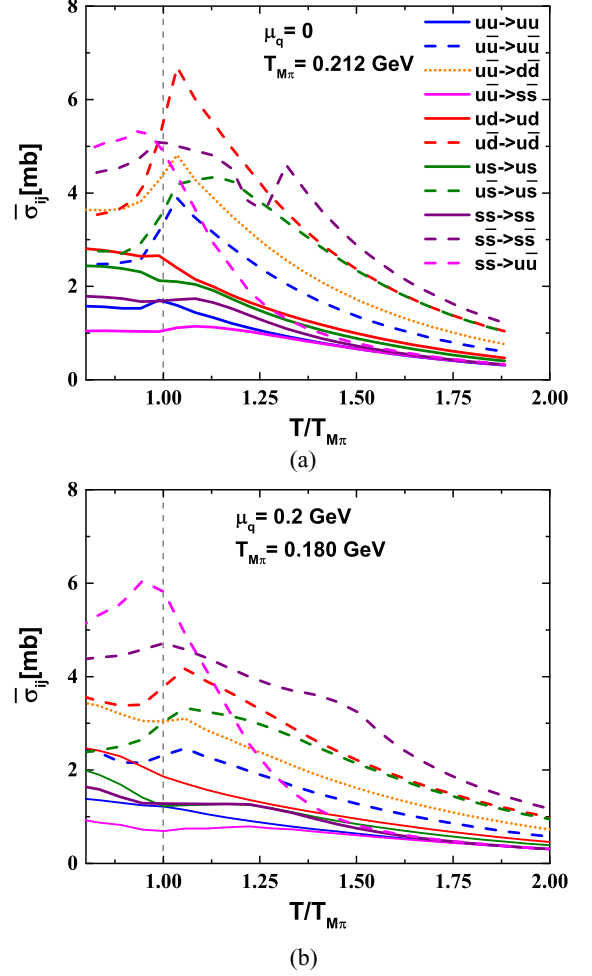


FIG. 15. “Weighted” thermal averaged total PNJL cross sections $\bar{\sigma}_{ij}(T, \mu_q)$ from Eq. (56) as a function of the scaled temperature $T/T_{M\pi}$ for (a) $\mu_q = 0$ (upper) and (b) $\mu_q = 0.2$ GeV (lower).

and the relative velocity in the c.m. frame is given by Eq. (50).

For the PNJL results we use also the modified Fermi-Dirac distribution function defined by Eq. (46). Quark densities with the modified Fermi-Dirac distribution functions are shown in Fig. 14 as a function of the temperature for (a) $\mu_q = 0$ and (b) $\mu_q = 0.2$ GeV.

The relaxation time for the light quarks is defined as

$$\tau_u^{-1}(T, \mu_q) = n_u(\bar{\sigma}_{uu \rightarrow uu} + \bar{\sigma}_{ud \rightarrow ud}) + n_{\bar{u}}(\bar{\sigma}_{u\bar{u} \rightarrow u\bar{u}} + \bar{\sigma}_{u\bar{u} \rightarrow d\bar{d}})$$

$$+ \bar{\sigma}_{u\bar{u} \rightarrow s\bar{s}} + \bar{\sigma}_{u\bar{d} \rightarrow u\bar{d}} + n_s \bar{\sigma}_{us \rightarrow us} + n_{\bar{s}} \bar{\sigma}_{u\bar{s} \rightarrow u\bar{s}}. \quad (58)$$

The relaxation time for strange quarks is defined as

$$\tau_s^{-1}(T, \mu_q) = 2n_u \bar{\sigma}_{us \rightarrow us} + 2n_{\bar{u}} \bar{\sigma}_{u\bar{s} \rightarrow u\bar{s}}$$

$$+ n_s \bar{\sigma}_{ss \rightarrow ss} + n_{\bar{s}}(\bar{\sigma}_{s\bar{s} \rightarrow s\bar{s}} + 2\bar{\sigma}_{s\bar{s} \rightarrow u\bar{u}}). \quad (59)$$

Figure 15 shows the “weighted” thermal averaged PNJL cross sections $\bar{\sigma}_{ij}(T, \mu_q)$ for different scattering processes as a function of the scaled temperature $T/T_{M\pi}$ for (a) $\mu_q = 0$ and (b) $\mu_q = 0.2$ GeV. $\bar{\sigma}_{ij}(T, \mu_q)$ shows a peak in the vicinity of the pion Mott temperature $T_{M\pi}$, which is more

pronounced for the quark-antiquark $q\bar{q}$ scattering due to the peak in the cross sections caused by the s -channel contribution (see the discussion in Sec. II F). Due to this increase of the $q\bar{q}$ cross sections the “weighted” thermal averaged cross sections $\bar{\sigma}_{ij}(T, \mu_q)$ for the $q\bar{q}$ channels dominate over the qq channels. Approaching high temperatures, above $T_{M\pi}$, the averaged cross sections $\bar{\sigma}_{ij}(T, \mu_q)$ decrease with temperature as expected from the behavior of the total PNJL cross sections presented in the previous section. The shape of “weighted” thermal averaged cross sections for $\mu_q = 0$ is similar to the NJL results presented in [19], while the absolute values of the PNJL “weighted” thermal averaged cross section $\bar{\sigma}_{ij}(T, 0)$ are larger due to different model parameters and due to the larger values of the effective quark masses.

Using Eqs. (53),(54) and (55),(56) one can compare the underlying differences of the two presented methods to calculate the quark relaxation time. The first approach is simply an averaging of $v_{\text{rel}} \cdot \sigma(\sqrt{s})$ over the momentum of the partons in the entrance channel. The second method requires in addition that the sum of the quark momenta in the entrance channel is zero and introduces an additional \sqrt{s} dependence by integrating over s instead of over \sqrt{s} . The first approach does not need any normalization whereas for the second method the normalization covers some of the parameter dependence of $P(s, T, \mu_q)$.

Figure 16(a) gives an overview of the relaxation times of light and strange quarks as a function of the scaled temperature $T/T_{M\pi}$ and for $\mu_q = 0$. The solid gray and the dashed orange lines correspond to the actual results from Eq. (55), where the “weighted” thermal averaged cross sections $\bar{\sigma}_{ij}$ are used. The solid blue and the dashed red lines correspond to the results from Eq. (54), where the averaged transition rates \bar{w}_{ij} are used.

The difference between the two methods is most prominently seen at high temperatures. Calculations of the quark relaxation time using the averaged transition rates are more straightforward since they rely on the relation between the momentum depended relaxation time and the interaction rate.

In addition, we compare the quark relaxation time $\tau_i(\bar{\sigma}_{ij})$ for the PNJL model with the results for $N_f = 3$ NJL model [19] (dashed magenta line). Our results are in a good agreement with the NJL results except for the vicinity of $T_{M\pi}$. The light quark relaxation time $\tau_i(\bar{\sigma}_{ij})$ in this case is about 0.7–0.5 fm/c in the region $T_{M\pi} \leq T \leq 1.8T_{M\pi}$.

The μ_q dependence of the quark relaxation time $\tau_i(\bar{w}_{ij})$ is shown in Fig. 16(b) for three values of μ_q : 0, 0.2, and 0.3 GeV. The solid lines correspond to the results for light quarks while the dashed lines correspond to the results for strange quarks. The quark relaxation time is increasing with the chemical potential μ_q in the region of $T \leq 2T_{M\pi}$. One can see that in the vicinity of the $T_{M\pi}$ the relaxation time for the strange quark is larger than for the light quark. This difference becomes more significant for finite μ_q due to the difference between the effective masses of light and strange quarks.

C. Shear viscosity

The most desired transport coefficients are the shear and bulk viscosities. They have been successfully used in the

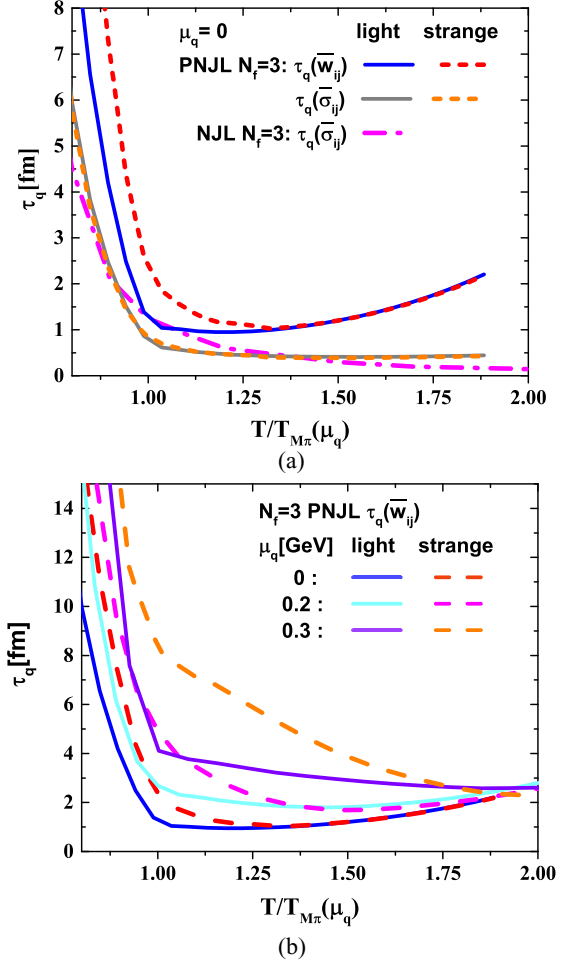


FIG. 16. Relaxation time of light and strange quarks as a function of the scaled temperature $T/T_{M\pi}(\mu_q)$ for (a) $\mu_q = 0$ (upper) and (b) $\mu_q \geq 0$ (lower). The solid and the dashed lines show the results for the PNJL model using the averaged transition rates \bar{w}_{ij} (54) and the “weighted” thermal averaged cross sections $\bar{\sigma}_{ij}$ (55).

viscous relativistic hydrodynamic description of the QGP bulk dynamics. In large systems the shear viscosity and the entropy density scale as T^3 . Therefore often the specific shear and bulk viscosities are used: the dimensionless ratio of the viscosity to the entropy density. The specific shear viscosity allows one to compare the viscosity of liquids at various temperature scales. The main contribution for the viscous description of the QGP comes from the shear viscosity. For this purpose we show the transport coefficients as a function of the scaled temperature T/T_C . For the PNJL calculations we use $T_C = T_{M\pi}$ whereas for the other approaches T_C is the temperature of the inflection point. Here we focus on the estimation of the transport coefficients based on the RTA.

The shear viscosity for quarks with medium dependent masses $M(T, \mu_q)$ can be derived using the Boltzmann equation in the RTA [42] through the relaxation time:

$$\eta(T, \mu_q) = \frac{1}{15T} \sum_{i=q,\bar{q}} \int \frac{d^3p}{(2\pi)^3} \frac{\mathbf{p}^4}{E_i^2} \tau_i(T, \mu_q) \cdot d_q f_i^\phi, \quad (60)$$

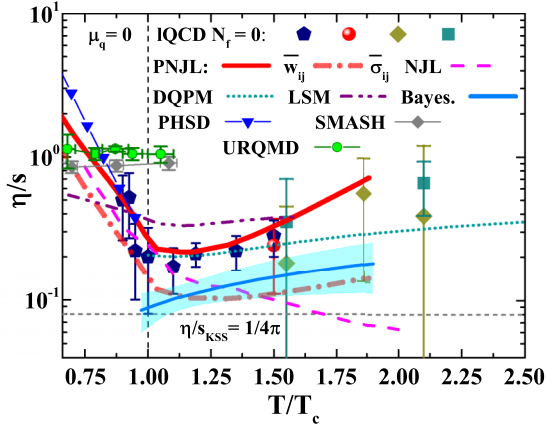


FIG. 17. Specific shear viscosity η/s as a function of scaled temperature T/T_c for $\mu_q = 0$. The solid and the dashed red lines show the results of the η/s for the PNJL model using the averaged transition rates \bar{w}_{ij} (54) and the averaged cross sections $\bar{\sigma}_{ij}$ (55) for the evaluation of the relaxation time. We show the estimations from various models: URQMD [48] (dotted green line), PHSD [49] (dotted green line), SMASH [50] (dotted green line), the $N_f = 2$ linear sigma model [51] (dashed-dotted purple line), the $N_f = 3$ NJL model [19] (dashed magenta line), and DQPM [21] (dotted green line). The dashed gray line demonstrates the Kovtun-Son-Starinets bound [52] $(\eta/s)_{\text{KSS}} = 1/(4\pi)$. The symbols show IQCD data for pure SU(3) gauge theory taken from Refs. [53] (squares and rhombus), [54] (circle), and [55] (pentagons). The solid blue line shows the results from a Bayesian analysis of experimental heavy-ion data [56].

where $q(\bar{q}) = u, d, s(\bar{u}, \bar{d}, \bar{s})$, τ_i are the relaxation times, and f_i^ϕ are the modified distribution functions, which contain the Polyakov loop contributions.

Figure 17 shows the scaled temperature dependence T/T_c of the specific shear viscosity η/s for $\mu_q = 0$. The solid and dashed red lines show the PNJL results from Eq. (60) using the two different estimations of the quark relaxation time: with the averaged transition rates \bar{w}_{ij} from Eq. (54) and with the “weighted” thermal averaged cross sections $\bar{\sigma}_{ij}$ from Eq. (55). The dashed gray line demonstrates the Kovtun-Son-Starinets bound [52] $(\eta/s)_{\text{KSS}} = 1/(4\pi)$, and the symbols show IQCD data for pure SU(3) gauge theory, taken from Refs. [53] (squares and rhombus), [54] (circle), and [55] (pentagons). The solid blue line presents an estimation of η/s from the Bayesian analysis of the experimental heavy-ion data from Ref. [56], which has a similar temperature dependence. The result of η/s (using $\bar{\sigma}_{ij}$) is twice smaller than η/s (using \bar{w}_{ij}) due to the different values of the quarks’ relaxation times.

We compare the results as well with those for the $N_f = 3$ NJL model from [19], where the relaxation time is estimated using Eq. (55) and with the DQPM prediction where the relaxation time is estimated using the on-shell interaction rate described by Eq. (48). As expected, η/s obtained within the second method is close to the NJL estimation, and differs only at high temperature due to small differences in the cross sections, while the first method predicts a higher value of η/s , which is remarkably close to the DQPM results and to the pure SU(3) gauge calculations. For the hadronic phase we show the estimations from various transport models: URQMD

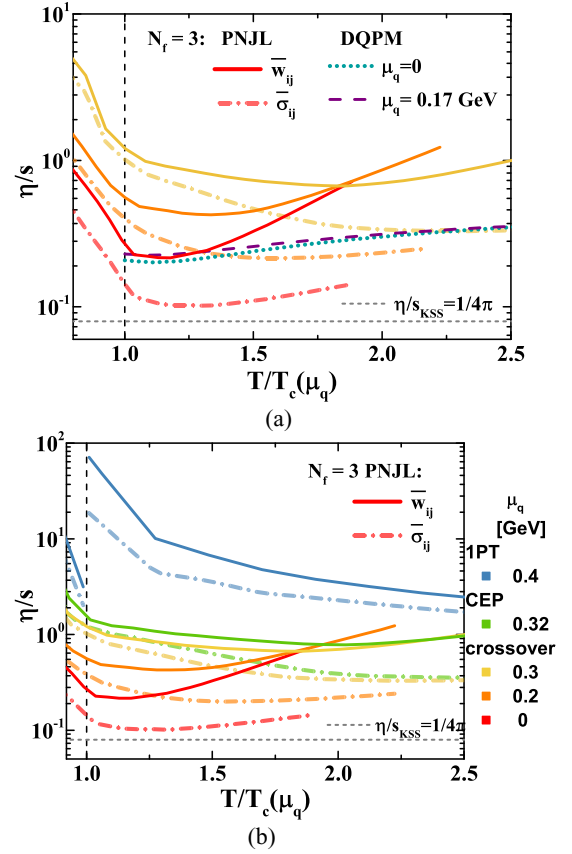


FIG. 18. Specific shear viscosity η/s as a function of scaled temperature T/T_c for (a) (upper) a moderate value of the quark chemical potential $0 \leq \mu_q \leq 0.3$ which corresponds to a crossover phase transition and (b) (lower) the whole range of the quark chemical potential $0 \leq \mu_q \leq 0.4$ GeV. The solid (dashed) red lines show the PNJL results of η/s for the PNJL model using the averaged transition rates \bar{w}_{ij} (54) [the averaged cross sections $\bar{\sigma}_{ij}$ (55)] for the evaluation of the relaxation time. The dotted green line and dashed purple line correspond to the results from the DQPM [21] for $\mu_q = 0$ and $\mu_q = 0.17$ GeV. The dashed gray line demonstrates the Kovtun-Son-Starinets bound [52] $(\eta/s)_{\text{KSS}} = 1/(4\pi)$.

[48] (dotted green line), PHSD [49] (dotted green line), and SMASH [50] (dotted green line). The PNJL results for the two methods show a similar temperature dependence in the vicinity of the chiral phase transition. Approaching the phase transition η/s has a dip, which is followed by an increase in the high temperature region. Later we consider results for nonzero chemical potential, where in the crossover region the DQPM calculations show a very moderate dependence on the chemical potential (for $\mu_u = \mu_s = \mu_B/3$), while the PNJL predictions have a more pronounced μ_q dependence. As we can see later, for the whole range of the quark chemical potential the two methods result in a similar temperature behavior when approaching the chiral phase transition.

Figure 18(a) depicts the specific shear viscosity for moderate values of the quark chemical potential $0 \leq \mu_q \leq 0.3$ GeV where the phase transition is a rapid crossover. We compare our results with the estimations from the DQPM for $\mu_q = 0$ (dotted green line) and $\mu_q = 0.17$ GeV (dashed violet line).

At moderate values of μ_q the specific shear viscosity shows a dip after the phase transition, which vanishes at high values of μ_q as can be seen in Fig. 18(b). For large μ_q , where the crossover transition turns into the first-order phase transition (IPT), the specific shear viscosity has a discontinuity near the critical temperature. In the vicinity of the CEP, for $\mu_q = 0.32$ GeV, there is a rather smooth change of η/s , which can be seen for the crossover phase transition at $\mu_q = 0.3$ GeV. So if one considers only μ_q values below the CEP, the temperature dependence of the specific shear viscosity cannot point out the position of the CEP. The evolution of the specific shear viscosity with μ_q is in qualitative agreement with previous findings made for the $N_f = 2$ NJL model in Ref. [47]. The numerical values differ due to the difference in the model parameters, distribution functions, and the NJL entropy density.

D. Electric conductivity

As QGP matter consists of charged constituents it is interesting to estimate the response of the system to an external stationary electric field. This is described by the electric conductivity σ_0 . Electric conductivity influences the soft photons spectra [57–59] and it is directly related to their emission rate [60]. The electric conductivity can be used for estimation the electromagnetic fields produced in heavy ion collisions [61].

The electric conductivity σ_0 of quarks with the effective masses $M(T, \mu_q)$ can be evaluated by using the relaxation time approximation (see Ref. [13]):

$$\sigma_0(T, \mu_q) = \frac{e^2}{3T} \sum_{i=q, \bar{q}} q_i^2 \int \frac{d^3p}{(2\pi)^3} \frac{\mathbf{p}^2}{E_i^2} \cdot \tau_i(T, \mu_q) d_q f_i^\phi, \quad (61)$$

where $e^2 = 4\pi\alpha_{em}$, $q_i = +2/3(u), -1/3(d), -1/3(s)$ are the quark electric charges, $d_q = 2N_c = 6$ is the degeneracy factor for spin and color in case of quarks and antiquarks, τ_i are their relaxation times, while f_i^ϕ denote the modified distribution functions for quark and antiquarks. In these formulas we deal with quarks and antiquarks of $N_f = 3$ flavors. Each quark has a contribution proportional to its charge squared. While viscosities have in general a gluonic contribution, the electric conductivity contains only a quark contribution.

The PNJL results for the dimensionless ratio of electric conductivity to temperature σ_0/T for $\mu_q = 0$ are presented in Fig. 19 for both methods of the calculation of the quark relaxation time as solid and dashed red lines. We compare the PNJL results to the various estimations from the literature: IQCD data for $N_f = 2$ taken from Refs. [62–64] (red circles with brown borders, yellow circles with green borders) and for $N_f = 2 + 1$ taken from Refs. [65,66] (spheres) and from Ref. [67] (blue stars), the kinetic partonic cascade model BAMPS [68] (dark-green solid line with triangles), the nonconformal holographic Einstein-Maxwell-dilaton (EMD) model [11] (dashed black line), the DQPM [21] (dotted green line); and below $T_c = 0.158$ GeV we show evaluations from hadronic models: the hadron resonance gas (HRG) model within the Chapman-Enskog expansion of the Boltzmann equation [14,69] (dashed cyan line), the $N_f = 2$ linear sigma model [51] (dashed-dotted purple line), and SMASH [70,71]

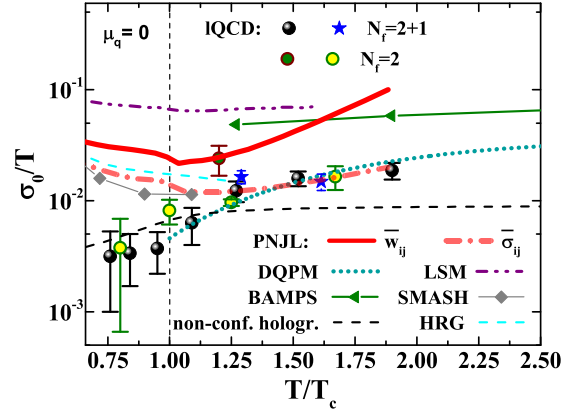


FIG. 19. Ratio of electric conductivity to temperature σ_0/T from Eq. (61) as a function of the scaled temperature T/T_c for $\mu_q = 0$. The solid (dashed) red lines show the PNJL results of σ_0/T for the PNJL model using the averaged transition rates \bar{w}_{ij} (54) [the “weighted” thermal averaged cross sections $\bar{\sigma}_{ij}$ (55)] for the evaluation of the relaxation time. The symbols display IQCD data for $N_f = 2$ taken from Refs. [62–64] (red circles with brown borders, yellow circles with green borders) and for $N_f = 2 + 1$ taken from Refs. [65,66] (spheres) and from Ref. [67] (blue stars). We compare to predictions from the various models: the kinetic partonic cascade model BAMPS [68] (the dark-green solid line with triangles), the nonconformal holographic EMD model [11] (dashed black line), the DQPM [21] (dotted green line), and below $T_c = 0.158$ GeV we show evaluations from hadronic models: the HRG model within the Chapman-Enskog expansion of the BU [14,69] (dashed cyan line), the $N_f = 2$ linear sigma model [51] (dashed-dotted purple line), and SMASH [70,71] (solid grey line with squares).

(solid grey line with squares). The PNJL results for the two methods of the estimation of quark relaxation time have a similar increase with temperature, which is mainly a consequence of the increase of the quark densities with temperature. The temperature dependence is in agreement with the predictions from the DQPM [21], despite the differences in the effective masses.

The chemical potential dependence is shown in Fig. 20(a) for moderate values of μ_q and 20(b) for the whole range of μ_q . As the specific shear viscosity, also the electric conductivity has a discontinuity at the first-order phase transition (and hence for $\mu_q > 0.32$). At lower chemical potentials, where the transition is a crossover, σ_0/T is a continuous function of the temperature. Starting from $\mu_q = 0$, with increasing μ_q , σ_0/T has first a dip approaching the phase transition temperature, which, for a moderate value of $\mu_q = 0.2$ – 0.3 GeV, turns into a hump; at $\mu_q = 0.4$ GeV, where the phase transition is of first order, it shows a discontinuity. For low values of μ_q and above the chiral phase transition, $T \leq 2T_c$, σ_0/T rises with μ_q , which is in agreement with the DQPM estimations [21] and predictions from the holographic calculations in Ref. [11].

It is interesting to compare the momentum diffusion, described by the specific shear viscosity η/s , and the charge diffusion, described by the scaled electric conductivity $\sigma_0/T = \kappa_Q/T^2$ (κ_Q is the charge diffusion coefficient) by calculating the ratio $\frac{\eta/s}{\sigma_0/T}$. This ratio is less dependent on the

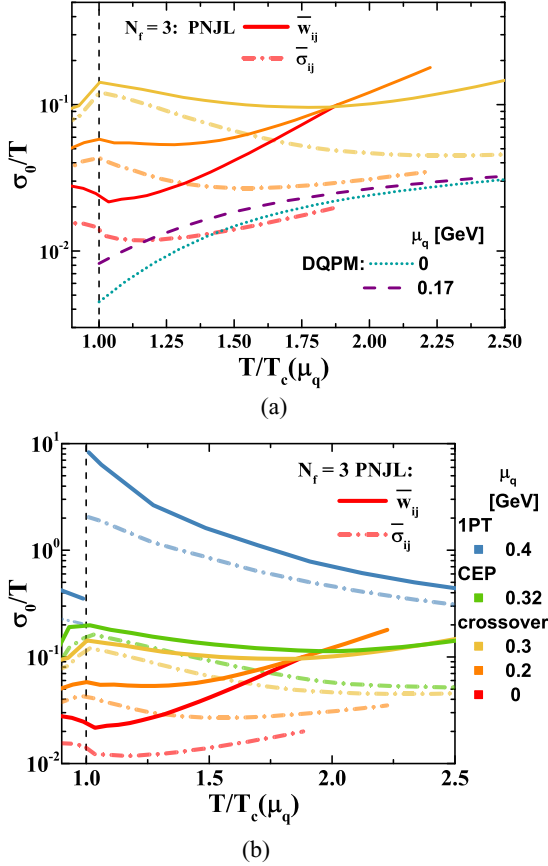


FIG. 20. Ratio of the electric conductivity to the temperature σ_0/T as a function of the scaled temperature T/T_C for (a) $\mu_q = 0$ (upper) and (b) $\mu_q \geq 0$ (lower). The solid (dashed) red lines show the PNJL results of σ_0/T for the PNJL model using the averaged transition rates \bar{w}_{ij} (54) [the “weighted” thermal averaged cross sections $\bar{\sigma}_{ij}$ (55)] for the evaluation of the relaxation time. The dotted green line and dashed purple line correspond to the results from the DQPM [21] for $\mu_q = 0$ and $\mu_q = 0.17$ GeV.

approximations made for the evaluation of the quark cross sections or quark relaxation times. The ratio $\frac{\eta/s}{\sigma_0/T}$ is presented in Fig. 21 as a function of scaled temperature T/T_C for a range of quark chemical potential $\mu_q \geq 0$.

For $\mu_q = 0$ we compare our results with the predictions from the anti-de Sitter/conformal field theory correspondence (AdS/CFT, grey dotted line) [52,73], evaluations from the $N_f = 2$ linear sigma model [51] (dashed-dotted purple line), the DQPM predictions [21] (green dash-dotted line), and estimation made in the quasiparticle (QP) model (blue dashed line) [72], where quarks and gluons are on-shell particles, and the coupling constant has a one-loop pQCD ansatz, which results in the higher parton masses compare to the DQPM masses. Note that the QPM has a higher value of the electric conductivity compared to the DQPM and IQCD results. For the PNJL calculations we see for μ_q values, where the theory shows a crossover, below T_C a strong decrease of this ratio with temperature, whereas above T_C the ratio flattens out. For μ_q values where a first-order phase transition is observed we see also for this ratio the discontinuity which we already observed for the viscosity and the electric conductivity.

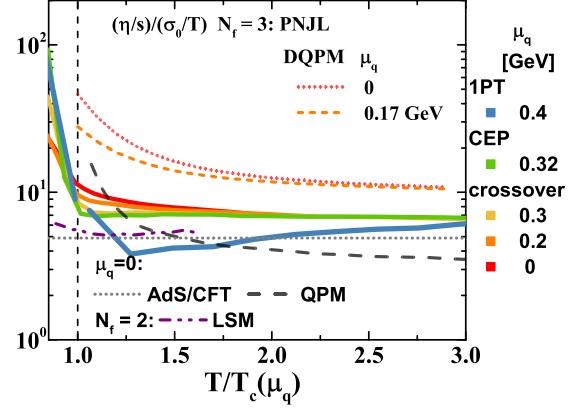


FIG. 21. Ratio of specific shear viscosity η/s to the scaled electric conductivity σ_0/T as a function of scaled temperature T/T_C for $\mu_q \geq 0$. For $\mu_q = 0$ we show the estimations from various models: the QP model [72] (dashed grey line), the DQPM [21] (dotted red line), the AdS-CFT [52,73] (dotted grey line), and the $N_f = 2$ linear sigma model [51] (dashed-dotted purple line).

It has to be mentioned that the three-dimensional mean field models are conceptually not accurate near the critical point and the first-order phase transition [74]. They are built on the ansatz that the fluctuations are small compared to the average value, while approaching the critical point the correlation length becomes large and diverges at the critical point. The feature of the PNJL and NJL models regarding the static critical exponents, the size of the critical region, and the influence of the Polyakov loop have already been studied in Refs. [75–77].

In the vicinity of the critical region one has to consider additional critical contributions governed by the dynamics of the fluctuations associated with the CEP. The dynamical universality class of the QCD critical point is argued to be that of the H model [78–80] according to the classification of dynamical critical phenomena by Hohenberg and Halperin [81]. Whereas in the vicinity of the CEP the shear viscosity has a mild divergence in the critical region, the bulk viscosity has a more pronounced divergence [80–83]: $\eta \sim \xi_T^{Z_\eta}$ ($Z_\eta \approx 1/19$), $\zeta \sim \xi_T^{Z_\zeta}$ ($Z_\zeta \approx 3$), and electric conductivity diverges as $\sigma_Q \sim \frac{1}{\xi_T^\nu}$, where $\xi_T \sim (T - T_C)^\nu$ is the thermal correlation length, with ν being the static critical exponent. The specific bulk and shear viscosities were considered near the CEP and the first-order phase transition for the $N_f = 2$ NJL model in the previous study [47]. Therefore the presented results can qualitatively describe η/s and σ/T above T_C , and a further development of the critical contribution to the transport coefficients in the critical region is needed. Recently a generic extension of hydrodynamics by a parametrically slow mode or modes (“Hydro+”) and a description of fluctuations out of equilibrium were considered in Ref. [84].

IV. CONCLUSION

We have calculated the specific shear viscosity η/s and the ratio of electric conductivity to temperature, σ_0/T , of QGP matter in the extended PNJL model for a wide range of quark

chemical potentials using the framework of the Boltzmann equation in the relaxation time approximation.

- (i) We showed that both the specific shear viscosity η/s and the ratio of the electric conductivity to the temperature, σ_0/T , depend strongly on the chemical potential.
- (ii) We demonstrated the dependence of the transport coefficients on the quark relaxation times, which were estimated with two methods: either by using the averaged transition rates \bar{w}_{ij} or by the “weighted” thermal averaged cross sections $\bar{\sigma}_{ij}$. The evaluation made within the first method is considered to be more realistic as it stems from the derivation of the relaxation time through the interaction rate.
- (iii) In the vicinity of the chiral phase transition the two methods result in a similar temperature dependence of the considered transport coefficients, which are, for a vanishing quark chemical potential, in agreement with various results from the literature. They include the results for the specific shear viscosity η/s and the ratio of the electric conductivity and the temperature, σ_0/T , obtained with the $N_f = 3$ NJL model [19], lattice QCD predictions, the $N_f = 2$ linear sigma model [51], predictions from the transport models such as URQMD, BAMPS, SMASH, PHSD, and estimations from the dynamical quasiparticle model [21]. In the vicinity of the pseudocritical temperature our results are remarkably close to that of IQCD calculations and to the results from the DQPM.
- (iv) The key result of this paper is the quark chemical potential μ_q dependence of transport coefficients. At moderate values of μ_q ($\mu_q \leq 0.3$ GeV), where the phase transition is a rapid crossover, transport coefficients show a smooth temperature dependence while approaching the (pseudo)critical temperature from the high temperature region.
- (v) At large values of μ_q the presence of a first-order phase transition changes the temperature dependence

of the transport coefficients drastically and a discontinuity can be seen when approaching the critical temperature.

- (vi) We found that the influence of the CEP on the evaluated transport coefficients is rather small in comparison to the modification due to a first-order phase transition. For the specific shear viscosity a similar behavior near the chiral phase transition has been obtained in the $N_f = 2$ NJL model in Ref. [47].
- (vii) We have considered furthermore the dimensionless ratio of specific shear viscosity to the scaled electric conductivity. It shows as well a discontinuity at T_C if the chiral transition is of first order but is otherwise almost constant for $T > 2T_C$.

To conclude, we have found a significant dependence of the value of the considered transport coefficients on the quark relaxation times evaluated by two different methods, which can explain the difference in the previously known RTA results from other models. Nevertheless, in the vicinity of the chiral phase transition the temperature and chemical potential dependence of the transport coefficients is similar for the two presented methods.

ACKNOWLEDGMENTS

The authors thank Wolfgang Cassing, Rudy Marty, Tae-soo Song, and Juan Torres-Rincon for useful discussions. O.S. acknowledge support from the “Helmholtz Graduate School for Heavy Ion research.” O.S. and E.B. acknowledge support by the Deutsche Forschungsgemeinschaft (DFG, German Research Foundation) through the grant CRC-TR 211 “Strong-interaction matter under extreme conditions,” Project No. 315477589-TRR 211. This work is supported by the European Union’s Horizon 2020 research and innovation program under Grant Agreement No. 824093 (STRONG-2020) and by the COST Action CA15213 THOR.

- [1] E. Shuryak, *Prog. Part. Nucl. Phys.* **62**, 48 (2009).
- [2] U. Heinz and R. Snellings, *Annu. Rev. Nucl. Part. Sci.* **63**, 123 (2013).
- [3] A. Adronic and P. Braun-Munzinger, K. Redlich, and J. Stachel, *Nature (London)* **561**, 321 (2018).
- [4] G. Odyniec (STAR Collaboration), *PoS (CORFU2018)*, 151 (2019).
- [5] P. Senger (CBM Collaboration), *Phys. Scr.* **95**, 074003 (2020).
- [6] D. Blaschke *et al.*, *Eur. Phys. J. A* **52**, 267 (2016).
- [7] P. Arnold, G. D. Moore, and L. G. Yaffe, *J. High Energy Phys.* **05** (2003) 051.
- [8] E. Shuryak, *Rev. Mod. Phys.* **89**, 035001 (2017).
- [9] S. Ryu, J.-F. Paquet, C. Shen, G. S. Denicol, B. Schenke, S. Jeon, and C. Gale, *Phys. Rev. Lett.* **115**, 132301 (2015).
- [10] M. Attems, J. Casalderrey-Solana, D. Mateos, I. Papadimitriou, D. Santos-Oliván, C. F. Sopena, M. Triana, and M. Zilhão, *J. High Energy Phys.* **10** (2016) 155.
- [11] R. Rougemont, R. Critelli, J. Noronha-Hostler, J. Noronha, and C. Ratti, *Phys. Rev. D* **96**, 014032 (2017).
- [12] G. Jackson and A. Peshier, *J. Phys. G* **45**, 095001 (2018).
- [13] L. Thakur, P. K. Srivastava, G. P. Kadam, M. George, and H. Mishra, *Phys. Rev. D* **95**, 096009 (2017).
- [14] M. Greif, J. A. Fotakis, G. S. Denicol, and C. Greiner, *Phys. Rev. Lett.* **120**, 242301 (2018).
- [15] V. Mykhaylova, M. Bluhm, K. Redlich, and C. Sasaki, *Phys. Rev. D* **100**, 034002 (2019).
- [16] Y. P. Zhao, *Phys. Rev. D* **101**, 096006 (2020).
- [17] A. Abhishek, A. Das, D. Kumar, and H. Mishra, *arXiv:2007.14757*.
- [18] D. Fuseau, T. Steinert, and J. Aichelin, *Phys. Rev. C* **101**, 065203 (2020).
- [19] R. Marty, E. Bratkovskaya, W. Cassing, J. Aichelin, H. Berrehrah, *Phys. Rev. C* **88**, 045204 (2013).
- [20] P. Moreau, O. Soloveva, L. Oliva, T. Song, W. Cassing, and E. Bratkovskaya, *Phys. Rev. C* **100**, 014911 (2019).

- [21] O. Soloveva, P. Moreau, and E. Bratkovskaya, *Phys. Rev. C* **101**, 045203 (2020).
- [22] A. Peshier and W. Cassing, *Phys. Rev. Lett.* **94**, 172301 (2005).
- [23] W. Cassing, *Nucl. Phys. A* **795**, 70 (2007); **791**, 365 (2007).
- [24] A. V. Friesen, Y. V. Kalinovsky, and V. D. Toneev, *Nucl. Phys. A* **923**, 1 (2014).
- [25] P. Zhuang, J. Hufner, S. P. Klevansky, and L. Neise, *Phys. Rev. D* **51**, 3728 (1995).
- [26] K. Fukushima, *Phys. Lett. B* **591**, 277 (2004).
- [27] E. Megias, E. R. Arriola, and L. L. Salcedo, *Phys. Rev. D* **74**, 065005 (2006).
- [28] C. Ratti, M. A. Thaler, and W. Weise, *Phys. Rev. D* **73**, 014019 (2006).
- [29] H. Hansler, W. M. Alberico, A. Beraudo, A. Molinari, M. Nardi, and C. Ratti, *Phys. Rev. D* **75**, 065004 (2007).
- [30] J. M. Torres-Rincon, B. Sintes, and J. Aichelin, *Phys. Rev. C* **91**, 065206 (2015).
- [31] S. P. Klevansky, *Rev. Mod. Phys.* **64**, 649 (1992).
- [32] P. Rehberg, S. P. Klevansky, and J. Hufner, *Nucl. Phys. A* **608**, 356 (1996).
- [33] P. Rehberg and S. P. Klevansky, *Ann. Phys. (NY)* **252**, 422 (1996).
- [34] P. Rehberg, S. P. Klevansky, and J. Hufner, *Phys. Rev. C* **53**, 410 (1996).
- [35] A. Bazavov *et al.* (HotQCD Collaboration), *Phys. Rev. D* **90**, 094503 (2014).
- [36] J. M. Torres-Rincon and J. Aichelin, *Phys. Rev. C* **96**, 045205 (2017).
- [37] A. Kurkela and A. Vuorinen, *Phys. Rev. Lett.* **117**, 042501 (2016).
- [38] E. Blanquier, Le modèle de Polyakov, Nambu et Jona-Lasinio et ses applications pour décrire les particules sub-nucléaires, Report No. tel-01099258, 2013TOU30159 (Toulouse III U., 2013).
- [39] P. Romatschke, *Phys. Rev. D* **85**, 065012 (2012).
- [40] P. Chakraborty and J. I. Kapusta, *Phys. Rev. C* **83**, 014906 (2011).
- [41] M. Alqahtani, M. Nopoush, and M. Strickland, *Phys. Rev. C* **92**, 054910 (2015).
- [42] M. Albright and J. I. Kapusta, *Phys. Rev. C* **93**, 014903 (2016).
- [43] J. L. Anderson and H. R. Witting, *Physica* **74**, 466 (1974).
- [44] A. Hosoya and K. Kajantie, *Nucl. Phys. B* **250**, 666 (1985).
- [45] H. Berrehrah, P. B. Gossiaux, J. Aichelin, W. Cassing, and E. Bratkovskaya, *Phys. Rev. C* **90**, 064906 (2014).
- [46] P. Deb, G. P. Kadam, and H. Mishra, *Phys. Rev. D* **94**, 094002 (2016).
- [47] C. Sasaki and K. Redlich, *Nucl. Phys. A* **832**, 62 (2010).
- [48] N. Demir and S. A. Bass, *Phys. Rev. Lett.* **102**, 172302 (2009).
- [49] V. Ozvenchuk, O. Linnyk, M. I. Gorenstein, E. L. Bratkovskaya, and W. Cassing, *Phys. Rev. C* **87**, 064903 (2013).
- [50] J. B. Rose, J. M. Torres-Rincon, A. Schäfer, D. R. Oliinychenko, and H. Petersen, *Phys. Rev. C* **97**, 055204 (2018).
- [51] M. Heffernan, S. Jeon, and C. Gale, *Phys. Rev. C* **102**, 034906 (2020).
- [52] P. K. Kovtun, D. T. Son, and A. O. Starinets, *Phys. Rev. Lett.* **94**, 111601 (2005).
- [53] A. Nakamura and S. Sakai, *Phys. Rev. Lett.* **94**, 072305 (2005).
- [54] S. Sakai and A. Nakamura, PoS (**LATTICE2007**), 221 (2007).
- [55] N. Astrakhantsev, V. Braguta, and A. Kotov, *J. High Energy Phys.* **04** (2017) 101.
- [56] J. E. Bernhard, J. S. Moreland, and S. A. Bass, *Nat. Phys.* **15**, 1113 (2019).
- [57] S. Turbide, R. Rapp, and C. Gale, *Phys. Rev. C* **69**, 014903 (2004).
- [58] Y. Akamatsu, H. Hamagaki, T. Hatsuda, and T. Hirano, *J. Phys. G* **38**, 124184 (2011).
- [59] O. Linnyk, W. Cassing, and E. L. Bratkovskaya, *Phys. Rev. C* **89**, 034908 (2014).
- [60] Y. Yin, *Phys. Rev. C* **90**, 044903 (2014).
- [61] L. Oliva, *Eur. Phys. J. A* **56**, 255 (2020).
- [62] B. B. Brandt, A. Francis, H. B. Meyer, and H. Wittig, *J. High Energy Phys.* **03** (2013) 100.
- [63] A. Francis, B. Brandt, H. Meyer, and H. Wittig, PoS (**Confinement X**), 186 (2013).
- [64] B. B. Brandt, A. Francis, B. Jäger, and H. B. Meyer, *Phys. Rev. D* **93**, 054510 (2016).
- [65] A. Amato, G. Aarts, C. Allton, P. Giudice, S. Hands, and J. I. Skullerud, *Phys. Rev. Lett.* **111**, 172001 (2013).
- [66] G. Aarts, C. Allton, A. Amato, P. Giudice, S. Hands, and J. I. Skullerud, *J. High Energy Phys.* **02** (2015) 186.
- [67] N. Y. Astrakhantsev, V. V. Braguta, M. D'Elia, A. Y. Kotov, A. A. Nikolaev, and F. Sanfilippo, *Phys. Rev. D* **102**, 054516 (2020).
- [68] M. Greif, I. Bouras, C. Greiner, and Z. Xu, *Phys. Rev. D* **90**, 094014 (2014).
- [69] J. A. Fotakis, M. Greif, C. Greiner, G. S. Denicol, and H. Niemi, *Phys. Rev. D* **101**, 076007 (2020).
- [70] J. Hammelmann, J. M. Torres-Rincon, J. B. Rose, M. Greif, and H. Elfner, *Phys. Rev. D* **99**, 076015 (2019).
- [71] J. B. Rose, M. Greif, J. Hammelmann, J. A. Fotakis, G. S. Denicol, H. Elfner, and C. Greiner, *Phys. Rev. D* **101**, 114028 (2020).
- [72] A. Puglisi, S. Plumari, and V. Greco, *Phys. Lett. B* **751**, 326 (2015).
- [73] S. Caron-Huot, P. Kovtun, G. D. Moore, A. Starinets, and L. G. Yaffe, *J. High Energy Phys.* **12** (2006) 015.
- [74] N. Goldenfeld, *Lectures on Phase Transitions and the Renormalization Group*, Frontiers in Physics Vol. 85 (Westview, Boulder, CO, 1992).
- [75] P. Costa, C. A. de Sousa, M. C. Ruivo, and Y. L. Kalinovsky, *Phys. Lett. B* **647**, 431 (2007).
- [76] P. Costa, C. A. de Sousa, M. C. Ruivo, and H. Hansen, *Europhys. Lett.* **86**, 31001 (2009).
- [77] B. J. Schaefer and M. Wagner, *Phys. Rev. D* **85**, 034027 (2012).
- [78] H. Fujii, *Phys. Rev. D* **67**, 094018 (2003).
- [79] H. Fujii and M. Ohtani, *Phys. Rev. D* **70**, 014016 (2004).
- [80] D. T. Son and M. A. Stephanov, *Phys. Rev. D* **70**, 056001 (2004).
- [81] P. C. Hohenberg and B. I. Halperin, *Rev. Mod. Phys.* **49**, 435 (1977).
- [82] L. P. Kadanoff and J. Swift, *Phys. Rev.* **166**, 89 (1968).
- [83] A. Onuki, *Phase Transition Dynamics* (Cambridge University Press, Cambridge, 2002).
- [84] M. Stephanov and Y. Yin, *Phys. Rev. D* **98**, 036006 (2018).